

AD-A251 060



DTIC
S ELECTE D
JUN 4 1992
C

(2)

CO₂ LASER FREQUENCY DOUBLING

FINAL REPORT

24 September 1991 - 24 April 1992

prepared for

NAVAL RESEARCH LABORATORY
4555 Overlook Avenue, SW
Washington, DC 20375-5001

Contract No. N00014-91-C-2279

prepared by

TEXTRON DEFENSE SYSTEMS
2385 Revere Beach Parkway
Everett, MA 02149

DISTRIBUTION STATEMENT A
Approved for public release;
Distribution Unlimited

92-14190



92 5 28 146

Table of Contents

	Page
1.0 Introduction and Summary	1
2.0 Selection of AgGaSe ₂	2
2.1 Frequency Doubling in AgGaSe ₂	3
2.2 Efficiency of Frequency Doubling	5
2.3 Doubling with Gaussian Pulses	6
2.4 Anticipated Nonlinear Coefficient of AgGaSe ₂	8
2.5 Crystal Specification	8
3.0 Selection of 9.55 μ m Line	13
3.1 Injection-Locking	13
3.2 Line Selection by Grating	15
4.0 Mode-Locking	19
4.1 Modulator Test	19
4.2 Theoretical Estimate of Mode-Locked Pulse Duration	23
4.3 Measurements of Mode-Locked Pulse Duration	24
4.4 Mode-Locking with Line Selection	29
4.5 Modulator Damage Threshold	31
5.0 Angular and Temperature Dependence of Phase-Matching	33
5.1 Intensity Dependence of Phase-Matching	36
6.0 Harmonic Generation with Short Pulse Trains	40
6.1 Harmonic Generation with Long Pulse Trains	43
6.2 Damage Threshold and Fluence Limitation	47
6.3 Optical Quality of Second Harmonic Beam	49
7.0 Thermal Conductivity of AgGaSe ₂	53
8.0 High Average Power Doubling	57
9.0 References	60



Statement A per telecon Barry Feldman
 NRL/Code 6540
 Washington, DC 20375-5000

NWW 6/2/92

Distribution/	
Availability Codes	
Avail and/or	Special
Dist	A-1

1.0 INTRODUCTION AND SUMMARY

This work addresses the possibility of a high average power coherent light source in the mid-infrared, specifically in the $4.8\text{ }\mu\text{m}$ atmospheric window. The approach is to frequency-double the $9.55\text{ }\mu\text{m}$ CO_2 laser line, yielding $4.775\text{ }\mu\text{m}$. In order to achieve efficient conversion, the intensity of the laser is increased by intracavity resonant modulation, or "mode-locking." The intensity for efficient conversion in typical available lengths of doubling material is at a minimum 20 MW cm^{-2} . However, the most efficient CO_2 lasers operate with a pulse duration of at least $1\text{ }\mu\text{sec}$, the characteristic time for energy transfer from N_2 to CO_2 at 1 atmosphere.⁽¹⁾ Without modulation a fluence of at least 20 J cm^{-2} would therefore be needed for high overall system efficiency. With modulation at a 1:10 or better mark-to-space ratio, this fluence is reduced to the 2 J cm^{-2} range that typifies the surface damage threshold of available materials.

One important unknown was the effect on damage threshold of a modulated versus an unmodulated pulse. Was the threshold dependent on peak intensity, or fluence?

Other questions related to the specific material AgGaSe_2 , silver gallium selenide, chosen for this work. What was the quality of the second harmonic beam; what was the effective nonlinear coefficient; what was the temperature dependence of the phase-matching; and what was its thermal conductivity (to remove absorbed heat in an average power situation)?

Experimentally a mode-locked pulse train was generated using a TEA CO_2 laser pumped for a duration of $3\text{ }\mu\text{sec}$, containing 1 nsec pulses spaced by 40 nsec . The $9.55\text{ }\mu\text{m}$ line was selected either by injection or by the use of an intracavity grating.

In a series of experiments at increasing fluence, integrated harmonic energy conversions of up to 78% were observed. The phase-matching angle was insensitive to temperature within the accuracy of our measurement, the second harmonic beam was diffraction-limited and the nonlinear coefficient that best fitted the data was $d_{36} = 31 \pm 4\text{ pm V}^{-1}$, in agreement with the most accurate literature measurements. An interesting observation was made of the increased angular sensitivity of phase-matching at high harmonic conversion.

The crystal surface damage threshold was established for long and short pulse trains of very different peak intensity. The damage was apparently dependent more strongly on fluence than intensity, and could be represented by

$$F_D \approx 2t^{0.25} \text{ Jcm}^{-2}$$

where F_D is the damage fluence and t is the pulse train duration in microseconds.

The crystal thermal conductivity was measured to be $0.012 \text{ W cm}^{-1} \text{ } ^\circ\text{C}^{-1}$, in directions perpendicular, and mostly parallel to, the c-axis. This is a rather low value, comparable to that for fused silica, or pyrex, and can be the cause of considerable crystal temperature gradients in an average-power application.

The selection of AgGaSe_2 and a summary of the theory of second harmonic generation are presented in Section 2. Laser line selection is discussed in Section 3. Short pulse generation by mode-locking is described in Section 4, which also includes a measurement of the pulse duration by autocorrelation. The angular and temperature dependence of phase-matching are discussed in Section 5 and the detailed comparison of theory and experiment are covered in Section 6, which also summarizes the damage measurement and details the beam quality measurements. In Section 7 we describe the thermal conductivity measurement. Conclusions relating to the use of AgGaSe_2 for efficient, high power generation in the $4.8 \text{ }\mu\text{m}$ band are presented in Section 8.

2.0 SELECTION OF AgGaSe₂

The nonlinear material silver gallium selenide (AgGaSe₂)^(2,3) was selected for these experiments because:

- a) It has a relatively high nonlinear coefficient.
- b) It is now available with very low absorption at 9.55 μm (or 10.6 μm).
- c) It is available in perfect single crystals of length up to 35 mm at 50° to the C-axis.
- d) It is chemically stable in room air.
- e) It has a relatively high optical damage threshold.

Other nonlinear materials that were considered are Tl₃AsSe₃ (TAS) which has been used for high efficiency doubling at 10.6 μm ,^(4,5) and ZnGeP₂.^(6,7) At present, there are still crystal quality problems in TAS,⁽⁵⁾ although an effective 3.3 cm length of material has been achieved and it has a very low absorption at 9.55 μm . The second harmonic beam quality was not quoted in References (4) and (5). ZnGeP₂ has an absorption in the 10 μm region, attributable to an optical phonon overtone, so that its use for high average power doubling is questionable.

2.1 Frequency Doubling in AgGaSe₂

The type I phase matching process⁽⁸⁾ is optimal for frequency doubling from 10.6 μm or 9.55 μm in AgGaSe₂. In this configuration the fundamental frequency is an ordinary ray and the second harmonic is an extraordinary ray. AgGaSe₂ is a negative uniaxial crystal with indices given by the following Sellmeier expression:

$$n^2 = A + \frac{B}{(1 - C/\lambda^2)} + \frac{D}{(1 - E/\lambda^2)}$$

where n is the refractive index and λ is the wavelength in microns.

The Sellmeier coefficients for AgGaSe₂ are given by Bhar,⁽⁹⁾ but we have found in the present work that they do not predict the correct phase-matching angle. The Kildal set of coefficients⁽¹⁰⁾ has been modified by

D. Roberts ⁽¹¹⁾ of Cleveland Crystals to encompass not only our present data but also parametric oscillator data from other laboratories. The Bhar and Roberts sets are listed in the following table.

INDEX	A	B	C	D	E
n _o	4.6453	2.2057	0.1879	1.8377	1600
ne	5.2912	1.3970	0.2845	1.9282	1600
n _o	3.9362	2.9113	0.15071	1.7954	1600
ne	3.3146	3.3616	0.14095	1.7677	1600

The type I phase-matching angle θ_m for frequency doubling is given by:

$$\sin^2 \theta_m = \frac{\left(\frac{1}{n_1^o}\right)^2 - \left(\frac{1}{n_2^o}\right)^2}{\left(\frac{1}{n_2^e}\right)^2 - \left(\frac{1}{n_2^o}\right)^2}$$

where subscripts 'o' and 'e' refer to ordinary and extraordinary rays, and subscripts '1' and '2' refer to the fundamental and second harmonic wavelengths. For doubling of the CO₂ P20 line at 9.55 μ m, the Bhar set gives $\theta_m = 50.11^\circ$, which is the angle to which our AgGaSe₂ crystal was cut (see specification below). During the experiments we found that $\theta_m = 48.86 \pm 0.4^\circ$ where almost all of the error relates to the quoted accuracy of the X-ray crystal orientation performed by Cleveland Crystals, the supplier. This experimental value was one of those used by Roberts to derive the above modified Sellmeier coefficients, which now give $\theta_m = 48.87^\circ$ for doubling at 9.55 μ m.

For later reference, the following indices are predicted by the Roberts coefficients:

$$n_1^o = 2.596881$$

$$n_1^e = 2.5649089$$

$$n_2^o = 2.615515$$

$$n_2^e = 2.582935$$

2.2 Efficiency of Frequency Doubling

The efficiency of doubling is usefully summarized by Eimerl.⁽¹²⁾ For plane waves the interaction of the first and second harmonics is mediated by a coupling constant C given by:

$$C = 5.46 d_{\text{EFF}} (\text{pm} / \text{V}) / (\lambda_1 (\mu\text{m}) n^{3/2})$$

where $d_{\text{EFF}} = d_{36} \sin \theta_m$ for type I doubling in AgGaSe₂ and the units of C are $\text{GW}^{-1/2}$. For a crystal of length L , the conversion efficiency is ⁽¹³⁾

$$\eta = \tanh^2 \left[\frac{1}{2} \tanh^{-1} (\text{sn} [2\eta_0^{1/2}, 1 + \delta^2 / 4\eta_0]) \right]$$

where

$$\eta_0 = C^2 I L^2$$

$$\delta = \left(\frac{1}{2} \right) \Delta k L$$

and sn is a Jacobi elliptic function. The units of the first harmonic intensity I are GW cm^{-2} for L in cm. δ is one half the phase mismatch between the second harmonic waves originating at the input and exit faces of the crystal.

For relatively low "drive parameters" $\eta_0 < 1$ the conversion efficiency is:

$$\eta = \eta_0 \left(\frac{\sin \delta}{\delta} \right)^2.$$

For larger drive parameters, at perfect phase matching ($\delta = 0$),

$$\eta = \tanh^2 (\eta_0^{1/2}).$$

The behavior of η for large drives η_0 and non-zero δ is discussed by Eimerl, who gives a useful contour map of conversion efficiency in η_0, δ space. The increased sensitivity of conversion to de-phasing at high drive

parameters is discussed below in Section 5.1 in relation to the present experiments in which the effect was quite noticeable.

2.3 Doubling with Gaussian Pulses

The mode-locked pulses of the present experiment have approximately Gaussian transverse and temporal intensity profiles. Provided that the birefringent "walk-off" is much less than the transverse size of the fundamental beam it is a good approximation to integrate the foregoing plane wave result across the range of intensities at different transverse positions in the beam. For our doubling process the estimated walk-off is 0.4 mm (in our 35 mm crystal) whereas the $1/e^2$ intensity radius ranged between 2 mm and 4 mm in the experiments.

The intensity can be written as:

$$I(r,t) = I_0 e^{-(\ell n 2)t^2/\Delta^2} e^{-2r^2/w^2}$$

where I_0 is the peak on-axis intensity, Δ is the HWHM pulse duration and w is the $1/e$ amplitude ($1/e^2$ intensity) radius of the beam.

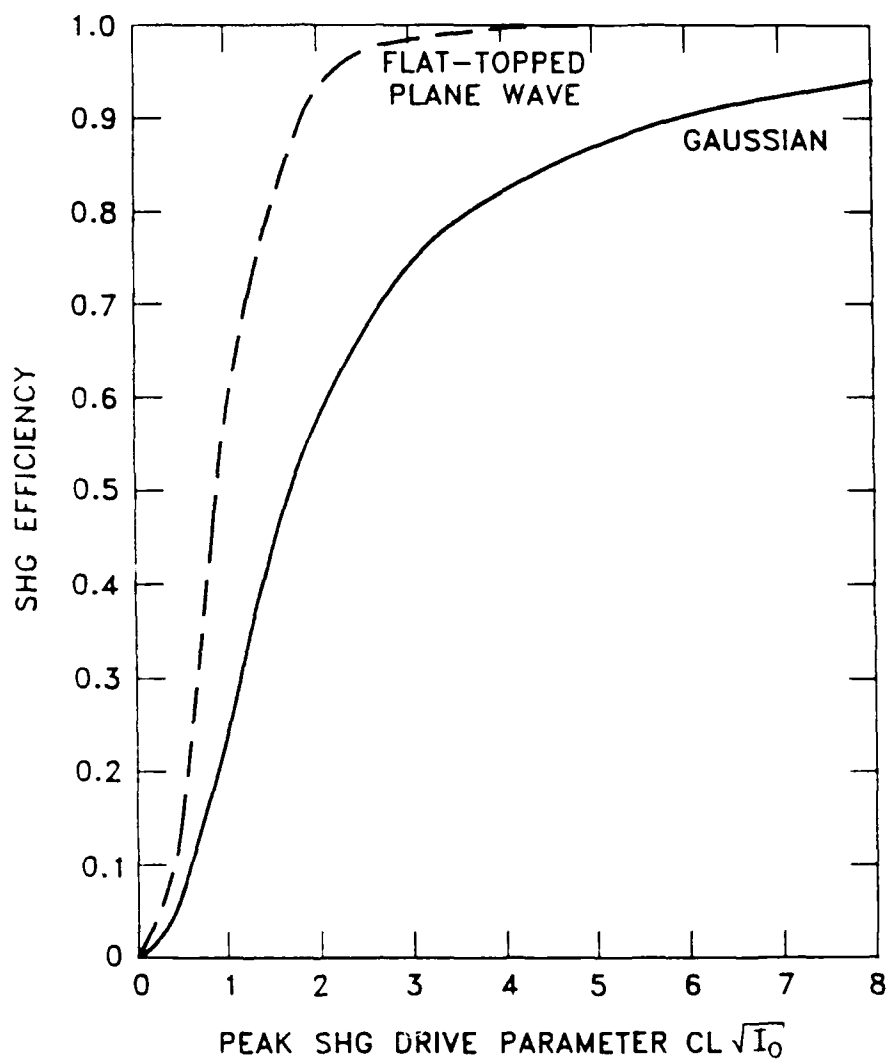
The energy in the pulse is:

$$\begin{aligned} E_p &= 2\pi \int_{-\infty}^{\infty} \int_0^{\infty} I(r,t) r dt dr \\ &= I_0 \pi^{3/2} \Delta w^2 / (2\sqrt{\ell n 2}) \end{aligned}$$

The time and space averaged second harmonic conversion efficiency is, for $\delta = 0$:

$$\eta = \frac{1}{E_p} \int_{-\infty}^{\infty} \int_0^{\infty} 2\pi r I(r,t) \tanh^2(\eta_0^{1/2}) dt dr$$

This function is shown vs $\eta_0^{1/2}$ in Figure 1 (labelled "Gaussian"). Also shown is the value of η for the flat-topped plane wave case discussed above in Section 2.2. This figure shows that, for example, to obtain 50% energy conversion with a Gaussian pulse requires about twice the drive parameter



P2435

Fig. 1 Second harmonic conversion efficiency as a function of the drive parameter $\sqrt{\eta_0} = CL\sqrt{I_0}$ where I_0 is the peak intensity in a spatial and temporal Gaussian profile. Dashed line shows constant plane wave case.

$\eta_0^{1/2}$ and about four times the intensity needed for the same conversion from a hypothetical flat-topped plane wave pulse.

Later, in comparing the measured conversion efficiency of pulse trains with theory, a range of different peak pulse intensities (I_0) has to be summed.

2.4 Anticipated Nonlinear Coefficient of AgGaSe₂

For AgGaSe₂ there is a range of d_{36} values in the literature. Values obtained by direct methods, and also one comparison measurement are listed in the following table which includes our present result:

$d_{36}(\text{pmV}^{-1})$	METHOD	REFERENCE
33 ± 4	Doubling $10.6\mu\text{m}$ in comparison with known d_{36} for GaAs	(2)
32.4 ± 5	Doubling 10.6μ , direct measurement	(10)
$43 \pm (?)$	Doubling $10.6\mu\text{m}$, direct measurement	(14)
$39 \pm (?)$	Parametric gain at $3.39\mu\text{m}$, direct measurement	(15)
31 ± 4	Doubling $9.55\mu\text{m}$, direct measurement	present work

The details of our present measurements are discussed in Section 6.0, where the data is fitted.

2.5 Crystal Specification

The following specification was agreed with Cleveland Crystals, in which θ is the polar phase-matching angle (Bhar Sellmeier used) and ϕ is the azimuthal phase-matching angle.

QTY.**DESCRIPTION**

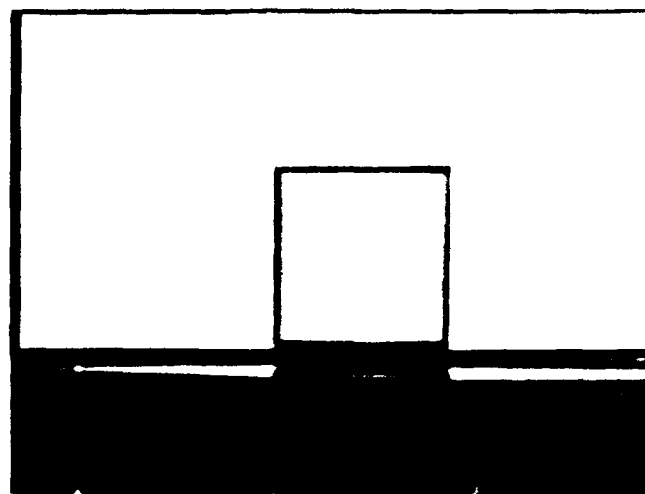
- | | |
|---|---|
| 1 | AgGaSe ₂ - 10 x 10 x 35 mm - I - $\phi = 45^\circ$, $\theta = 50.11^\circ$
SHG - 9.550/4.775 μm
Single Crystal
Polish (80% of aperture):
Flatness - best efforts
Parallelism $\sim \pm 15$ arc-seconds
Surface Roughness $\sim 25 \text{ \AA}$ rms - best efforts
AR "VV" coated both surfaces for 9.550 and 4.775 μm
No major inclusions and best effort on minimum of
minor inclusions (major inclusion size is greater than
50 μm) |
| 1 | Calorimetric Absorption Measurement at 10.6 μm |
| 1 | Profilometry (Surface Roughness) |
| 1 | IR Photography (NIR Broadband, B&W) showing
propagation direction and also a photo of the slab
before cutting to five the location of the crystal in the
boule and verify its single crystal nature |

Shipping Schedule: 6 Weeks ARO

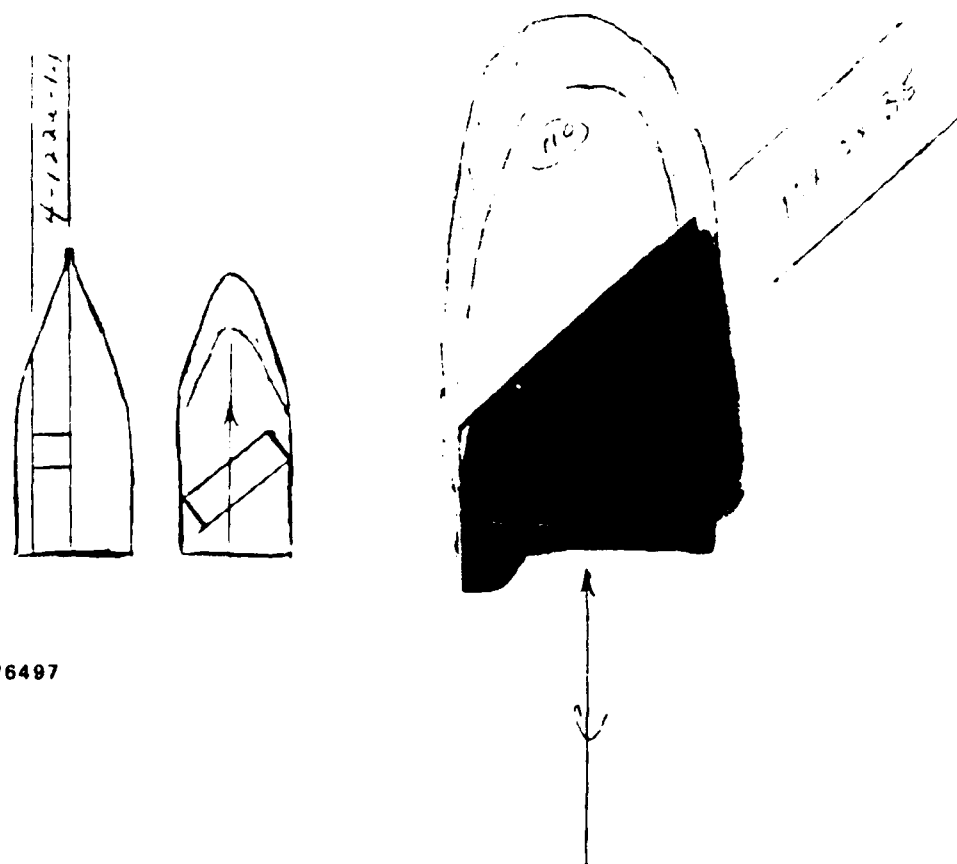
The crystal was delivered on schedule accompanied by the following data:

1. Infrared photograph at 1 μm showing absence of inclusions (Figure 2 (a)).
2. Sketch showing location of crystal cut in boule (Figure 2 (b)).
3. Surface Profiles at a number of locations in the central 80% of the crystal aperture (Figure 3), showing approx. 20 \AA r.m.s. finish.

The absorption at 10.6 μm was measured to be 0.012 cm^{-1} by Cleveland Crystals. In order to evaluate the "VV" anti-reflection coatings, we ran the crystal on a Perkin Elmer infrared spectrophotometer. At 9.55 μm and at 4.775 μm the transmission was $90\% \pm 2\%$. An additional



(a)



(b)

Fig. 2 (a) Near infrared photograph through the AgGaSe_2 crystal, showing absence of major inclusions or crystal boundaries. (b) Sketch to show cut of crystal within boule.

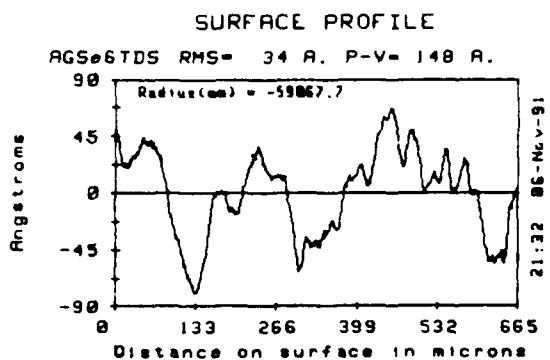
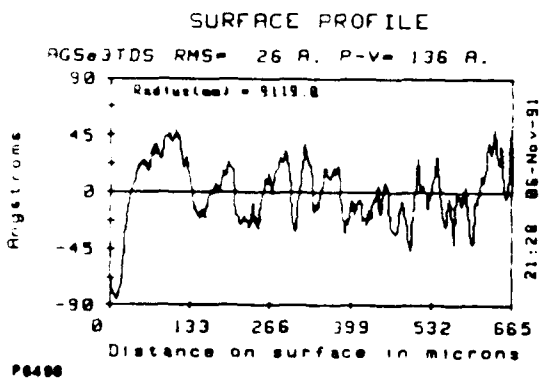
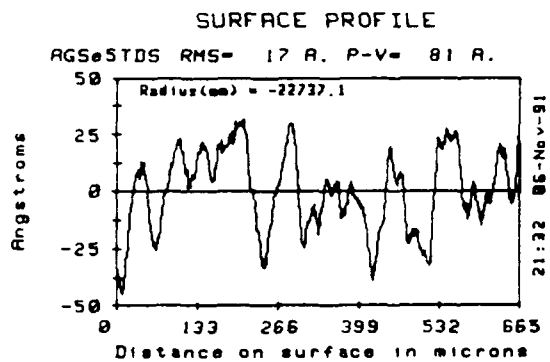
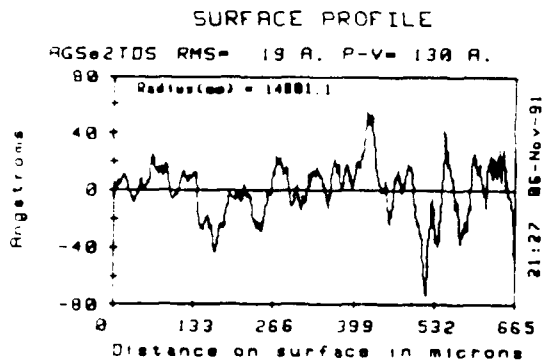
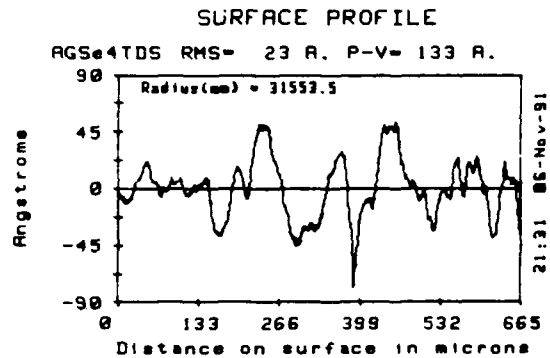
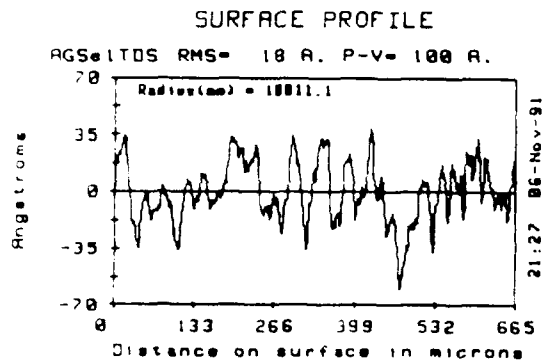


Fig. 3 Surface profilometry showing 25 Å RMS finish after polishing.

measurement with the polarized C.W. laser at $9.55\text{ }\mu\text{m}$ gave a transmission of $92.5\% \pm 1\%$. Considering the absorption loss of 4% at $10.6\text{ }\mu\text{m}$, which is probably the same at $9.55\text{ }\mu\text{m}$ because residual "absorption" in AgGaSe_2 is spectrally featureless ⁽¹⁶⁾ (possibly due to scattering by fine inclusions), the coatings were contributing a loss of about 2% at each surface at $9.55\text{ }\mu\text{m}$. Because scattering increases at reduced wavelength, it is likely that the "absorption" was at least 4% at $4.775\text{ }\mu\text{m}$ and that the coatings each reflected less than 3% at this wavelength. The coatings themselves consisted of a multilayer combination of lead and thorium fluorides. In Section 6.2, the optical damage threshold of the coatings is given for various incident pulse train profiles.

3.0 SELECTION OF 9.55 μm LINE

The selection of the 9.55 μm P20 CO₂ laser line was performed by either line injection of a CW laser, or by grating tuning. Both techniques yielded comparable mode-locked pulse durations but the grating technique proved simpler and more reliable. Injection had first been considered as a technique for eliminating the gain-switched "spike" in order to obtain multiple-microsecond pulse trains, for harmonic generation, of relatively uniform pulse intensity. Although this was achieved with very careful "tuning," and a feedback monitor to establish resonance, the practical usefulness of the approach was not adequate. By changing the gas mixture, carefully setting the cavity gain and amplifying the "tail" only, satisfactory long pulse waveforms were obtained with much better reliability from the grating-tuned laser.

3.1 Injection-Locking

The arrangement for injection-locking is shown in Figure 4. A CW CO₂ laser gave an output of 2 W in a TEM₀₀ mode at 9.55 μm . The CW beam was allowed to expand for a distance of 427 cm before passage through a 500 cm collimating lens. The beam emerged parallel, with a calculated $1/e^2$ spot parameter of 0.29 cm, slightly smaller than the 0.46 cm oscillator spot parameter at the output mirror of the oscillator, where injection occurred. A 95% transmitting beam splitter was used to direct 0.2 W of CW power into the oscillator (or at least in the direction of the oscillator). The same beam splitter transmitted 95% of the oscillator output for use in the experiment, and although 5% of the output was focussed back to the CW laser, the fluence there was never more than 0.2 J cm⁻², so the CW laser optics did not suffer damage.

The P20 9.55 μm line has less gain than about 10 of the 10.4 μm band lines and several other 9.4 μm band lines.⁽¹⁷⁾ Without line selection the CO₂ laser emits 10.6 μm - a line with a gain of 1.15 times that at 9.55 μm . Gain on the 10.4 μm band could be reduced by the use of a thin CaF₂ window at Brewster angle within the oscillator cavity. The 0.92 mm thick window at incidence angle 54.3° transmitted an estimated 64% at 10.6 μm , and 91% at 9.55 μm , completely suppressing all 10.4 μm band emission.

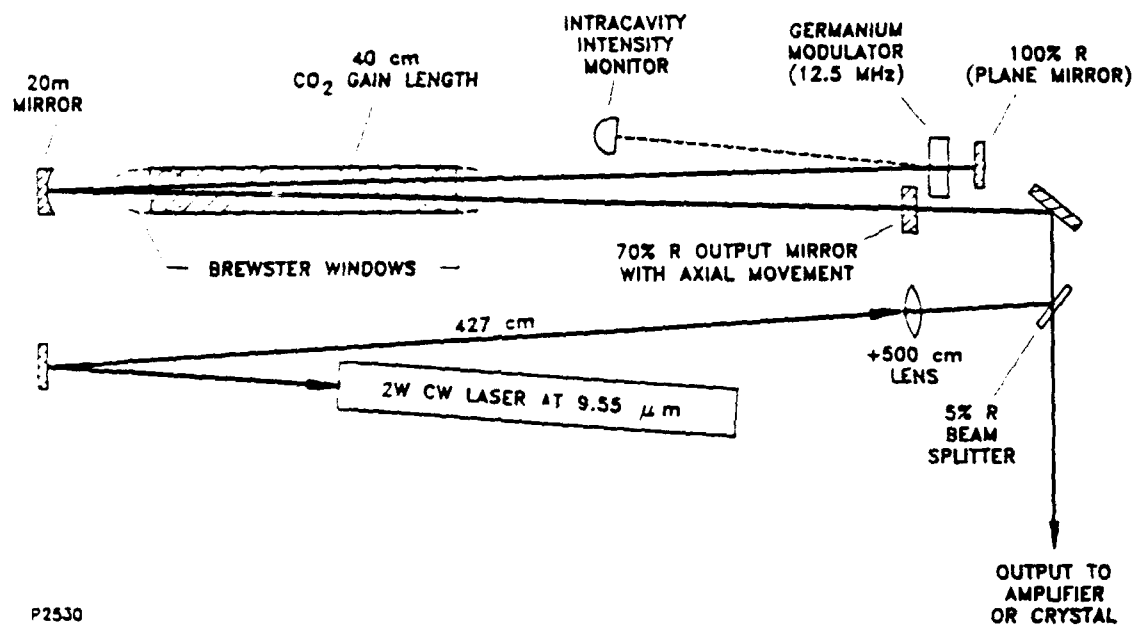


Fig. 4 Optical arrangement for the injection-locking of the CO₂ oscillator at 9.55 μ m.

With the CaF_2 window but no other line selection, emission was mostly on the P18 and P16 lines of the $9.4\text{ }\mu\text{m}$ band, with only occasional emission on the desired P20 line.

Line selection via injection was found to depend on careful angular alignment and on fine tuning of the oscillator cavity length to within a fraction of the CO_2 laser wavelength. The latter adjustment was performed manually via a fine linear drive which carried the laser output mirror. A problem was that this adjustment would only persist for at best a few tens of seconds, before either vibrations or thermal changes altered the cavity length. In order to achieve predictable results a monitor of the intracavity injected intensity was set up, consisting of a chopper and pyroelectric detector positioned to intercept the reflection off one face of the modulator (slightly tilted to the cavity axis). When this monitor signal had been optimized by fine tuning of the cavity length, the oscillator pulse was always line-locked. Varying degrees of optimization were employed to generate the range of pulse waveforms illustrated in Figure 5. The ratio of "spike" to "tail" intensities could be reduced to less than 3:1 in the best case. In this case the delay to oscillator output was reduced to $2.0\text{ }\mu\text{sec}$, whereas with no injection this delay lengthened to $3.0\text{ }\mu\text{sec}$ (and the $9.55\text{ }\mu\text{m}$ energy reduced almost to zero).

3.2 Line Selection by Grating

A standard high power CO_2 laser grating was obtained from Milton Roy of Rochester, NY. It was gold-coated, had 100 grooves per mm and was blazed for $9.5\text{ }\mu\text{m}$, at which wavelength its reflectivity was nominally greater than 95%. The incidence angle for $9.5\text{ }\mu\text{m}$ is 25.5° .

Neighboring CO_2 laser lines, P18 and P22, are reflected with an angular deviation of 0.04° which translates after a single 600 cm round trip to a lateral displacement of 0.4 cm, which equals nearly half of the mode-selection aperture diameter and therefore gives heavy losses. Over the 3 GHz bandwidth of the P20 line itself the displacement after one round trip is only 0.02 cm, so that about 10 round trips would be required to introduce only a few percent of loss. The grating therefore does not significantly narrow the laser spectrum within a given line.

As expected, the gain-switched "spike" dominates the laser output (for the $3\text{ }\mu\text{sec}$ PFN that we are using) as shown in Figure 6 (a). By

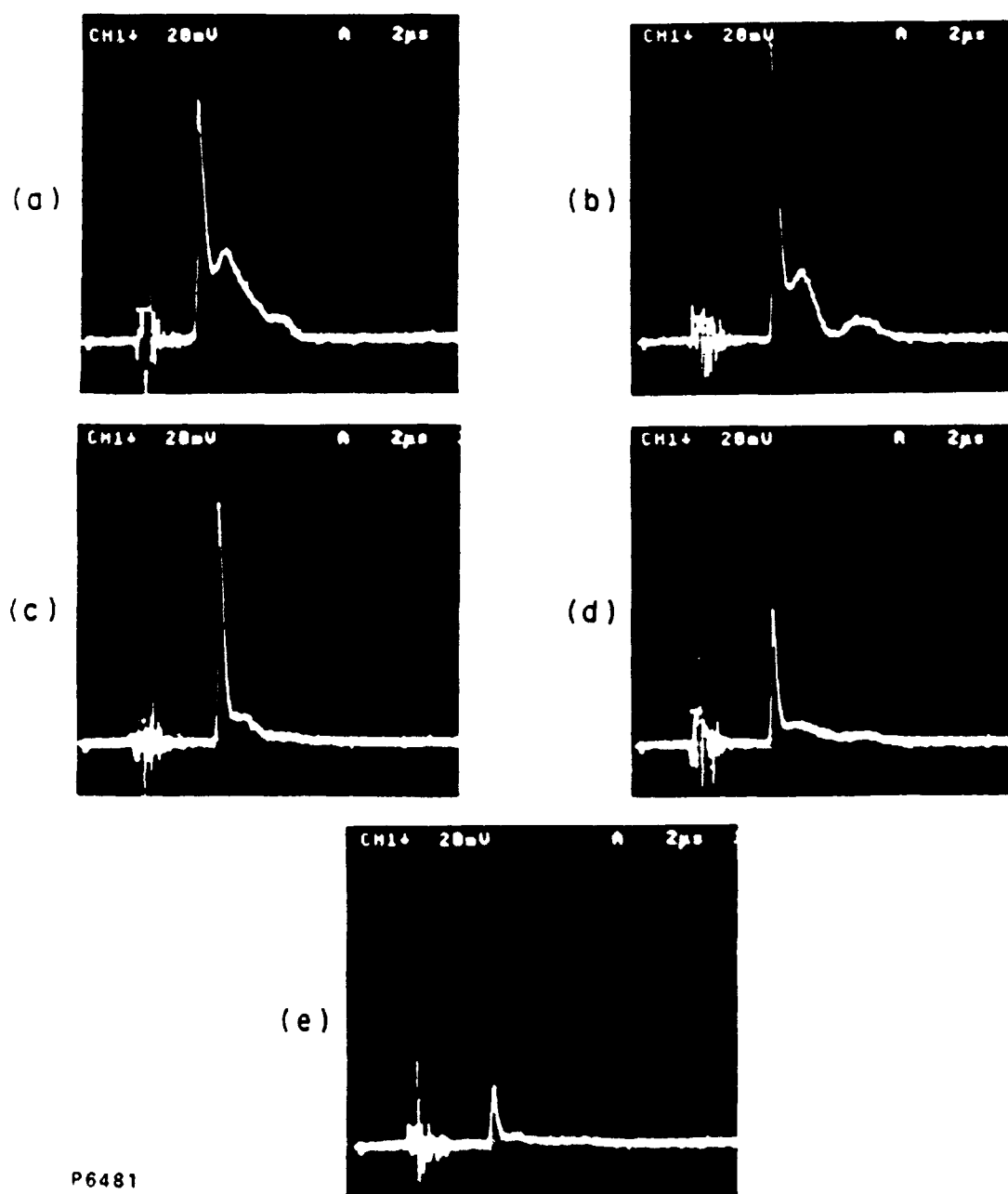
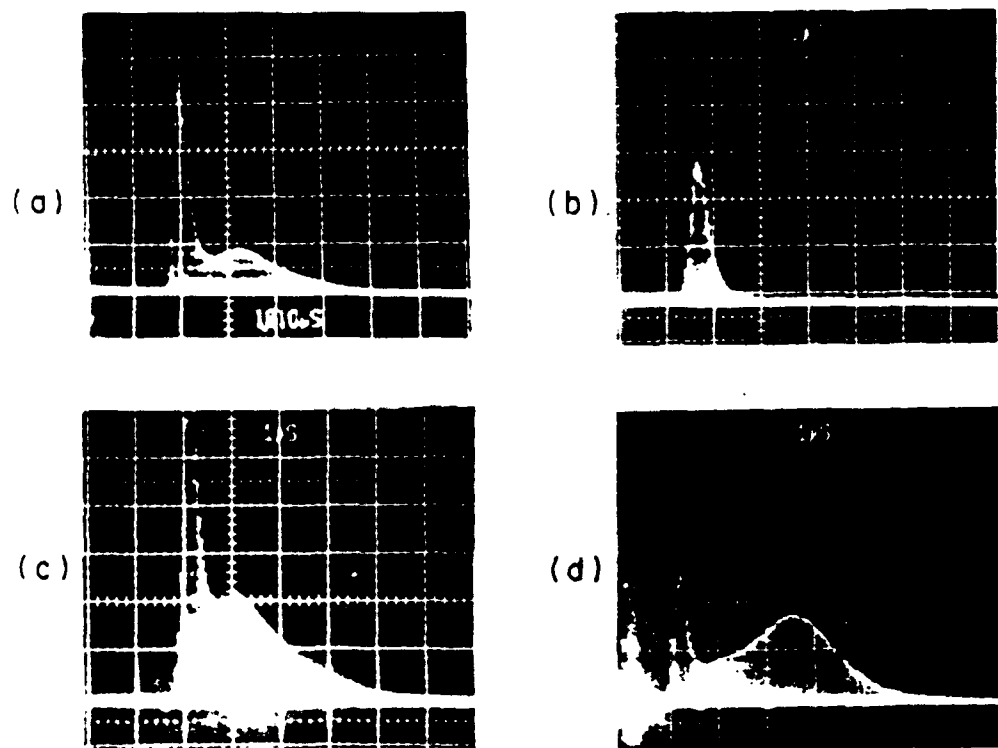


Fig. 5 9.55 μm output intensity profiles of injected laser with various degrees of cavity length matching: - (a) best length match; (b) --> (d) decreasing quality of match; (e) no injection.



P6480

Fig. 6 Different mode-locked pulse train envelopes achieved with combinations of a grating-tuned oscillator and amplifier: - (a) maximum oscillator aperture consistent with TEM_{00} mode; (b) reduced oscillator aperture; (c) oscillator output with enhanced N_2 in mix; (d) output (c) amplified with a $2.5 \mu\text{sec}$ delay.

reducing the mode-selection aperture, the cavity losses could be increased to the extent that lasing ceased immediately after the spike (Figure 6 (b)) leaving a useful short pulse train for harmonic generation at high intensity and low fluence. By increasing the nitrogen content of the mix (from our standard He:CO₂:N₂ = 8:2:1 to 7:2:2) the "tail" could be enhanced relative to the spike (Figure 6 (c)); and following amplification with a 2.5 μsec delay on the amplifier trigger pulse, the train could be dominantly "tail" as shown in Figure 6 (d). The latter pulse train was useful for the demonstration of harmonic generation at moderate intensity and high fluence.

4.0 MODE-LOCKING

The unmodulated pulsed CO₂ laser emits a noisy pulse train, in which there is periodicity at the cavity round trip time period. Examples for the present oscillator are shown in Figures 7(a) and 7 (b). The duration of individual "spikes" within the train is approximately 2 nsec. This number is the result of gain narrowing of the laser spectrum during the pulse buildup from noise. The spontaneous emission bandwidth of a 1 atmosphere CO₂ laser is about 3 GHz, so that an initial noise pulse duration of 0.1 nsec must have existed.

We employed amplitude modulation using diffraction off an acoustic wave in a germanium crystal. The availability of an oscillator, amplifier and several Ge crystals with transducers at 12.5 MHz dictated our choice of cavity round trip time (40 nsec) and modulation frequency. The acoustic wave amplitude falls to zero twice in each cycle, so that an effective 25 MHz (= 40 nsec) frequency is achieved.

4.1 Modulator Test

The modulators were characterized in a separate benchtop test in which a 3W CW 9.55 μ m beam was passed through the modulator and then a small iris at 3 m beyond the modulator. The transmitted intensity decreased as a function of RF power to the modulator as shown in Figure 8.

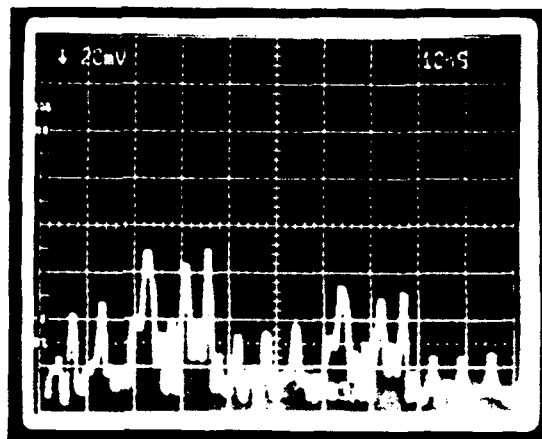
The "diffraction efficiency" is given by:

$$\frac{I_1}{I_0} = \sin^2 \left[\frac{\pi^2}{2} M_2 P_A \frac{L^2}{\lambda^2} \right]^{1/2}$$

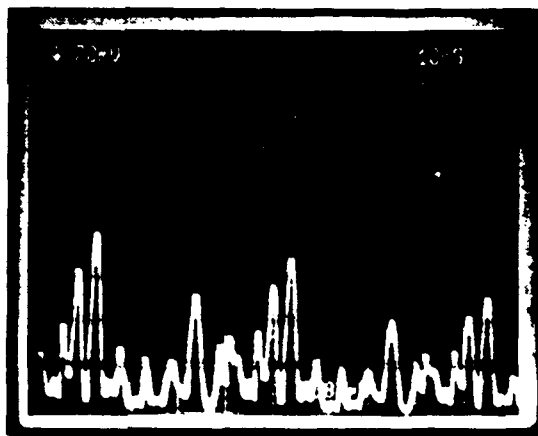
where

I_1	=	diffracted power
I_0	=	incident power
P_A	=	acoustic power density (ergs cm ⁻² sec ⁻¹)
$M_2(\text{Ge})$	=	8.1×10^{-16} sec ³ g ⁻¹
L	=	length (cm) through Ge crystal (optical direction)
λ	=	wavelength of incoming light (cm)

(a)



(b)



P6479

Fig. 7 Spontaneous modulation of the grating-tuned CO₂ laser output intensity. 40 nsec periodicity is seen in each example.

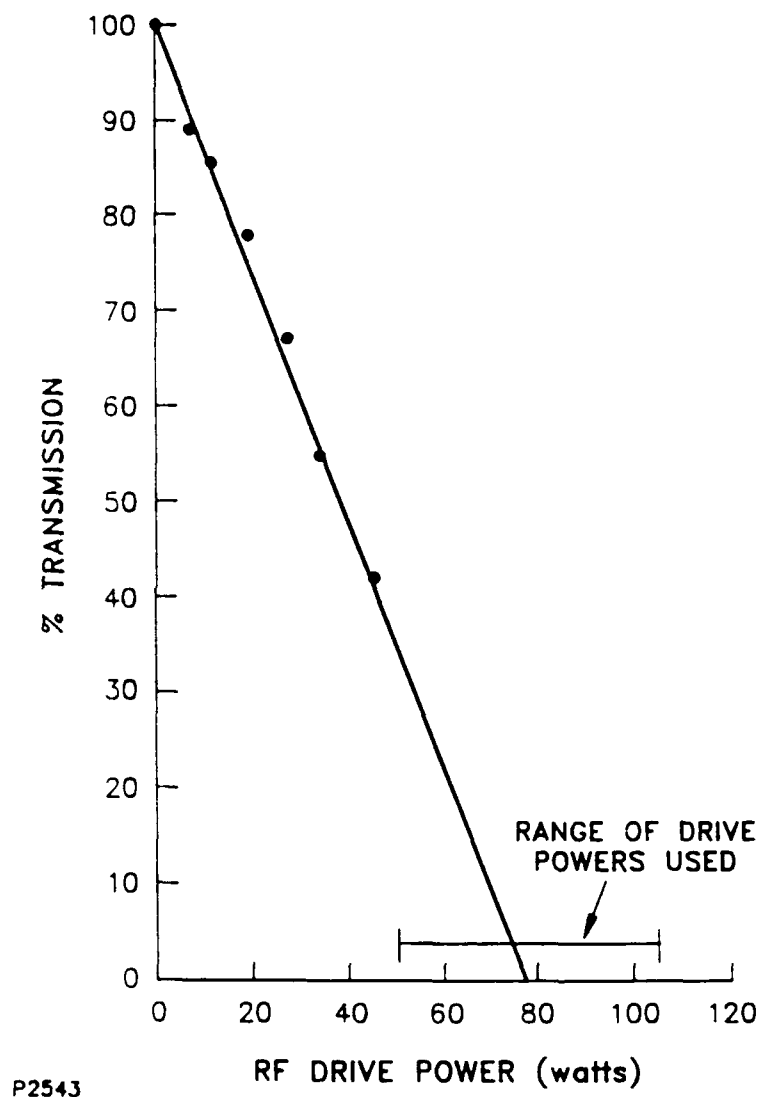


Fig. 8 Transmission of the undeflected component of a 9.55 μm CW laser as a function of modulator RF drive power.

The above formula is correct in the "Bragg regime" for which:

$$\frac{4\lambda L}{\Lambda^2} \gg 1$$

where Λ = acoustic wavelength. For Ge the speed of sound is 5.5×10^5 cm sec⁻¹ in the 111 direction which has the highest acousto-optical figure of merit M_2 for light polarized in the 111 direction.⁽¹⁸⁾ At 12.5 MHz the acoustic wavelength is therefore $\Lambda = 0.044$ cm. The available crystals had $L = 1$ cm, hence:

$$\frac{4\lambda L}{\Lambda^2} = 2.0$$

and the Bragg regime applied.

The benchtop modulator test measured the time-averaged diffraction efficiency due to an acoustic standing wave. In such a case the diffraction efficiency is periodic in time and an average has to be taken. The acoustic power density P_A is proportional to the square of the acoustic amplitude, and the standing wave amplitude goes as $\sin(w_s t)$ where w_s is the acoustic angular frequency. Therefore, the functional form of the diffraction efficiency with time is:

$$\frac{I_1}{I_0} = \sin^2[k_A \sin(w_s t)]$$

Averaging over one half acoustic period, and changing variables to $y = k_A \sin w_s t$:

$$\frac{2w_s}{\pi} \int_0^{\frac{\pi}{2w_s}} \frac{I_1}{I_0} dt = \frac{2}{\pi} \int_0^{k_A} \frac{\sin^2 y}{\sqrt{1-y^2}} dy$$

From the modulator test, for example, a time-averaged diffraction efficiency of 50% is observed at a modulator power of 26 Watts, and this corresponds to $k_A = 0.55$.

4.2 Theoretical Estimate of Mode-Locked Pulse Duration

From the model of Kuizenga et al.⁽¹⁹⁾ the mode-locked laser emits pulses of (FWHM) duration:

$$\tau_p = \sqrt{\frac{\ell n 2}{2}} \frac{1}{\pi} \frac{1}{\theta_m \sqrt{M f_m}}$$

where

- M = number of round trips during "buildup"
- θ_m = depth of modulation
- f_m = modulator frequency (here $f_m = 12.5$ MHz)

This result applies to the "transient" case, before a bandwidth-limited pulse is formed, and it can be shown that the present work is in this regime.

The single pass modulator transmission assumed by Kuizenga is:

$$f(t) = \cos^2(\theta_m \sin w_m t).$$

For an acoustic standing wave we observed (above) a deflected intensity:

$$I_1 = I_0 \sin^2(k_A \sin w_s t),$$

or a transmitted intensity of:

$$I_1 = I_0 \cos^2(k_A \sin w_s t),$$

implying the identity $\theta_m = k_A$ for the modulation depth. k_A is already known from the above modulator test (Section 4.1).

The duration of individual mode-locked pulses was measured using fast photodetectors at different points in the pulse train and at different depths of modulation. In the case of short pulse trains, consisting of only about 10 pulses, in the gain-switched spike, the duration was also measured in a second harmonic autocorrelation experiment. Overall, a rough agreement was observed between measured and theoretically-predicted pulse durations. The data is summarized and compared with theory in Table 1. The measured pulse duration was always less than the predicted, by a factor of 0.6 - 0.7, for reasons not understood at present.

Table 1
Comparison of Predicted and Measured Pulse Durations
for Amplitude-Modulated CO₂ Laser

Depth of Modulation θ_m	Number of Round Trips from Start of Gain (M)	Predicted Pulse Duration τ_p (nsec)	Measured Pulse Duration (nsec)
0.55	50	3.2	2.4
0.55	100	2.3	1.7
0.60	50	2.9	1.9
0.60	100	2.1	1.4
1.0	60	1.6	0.9-1.0

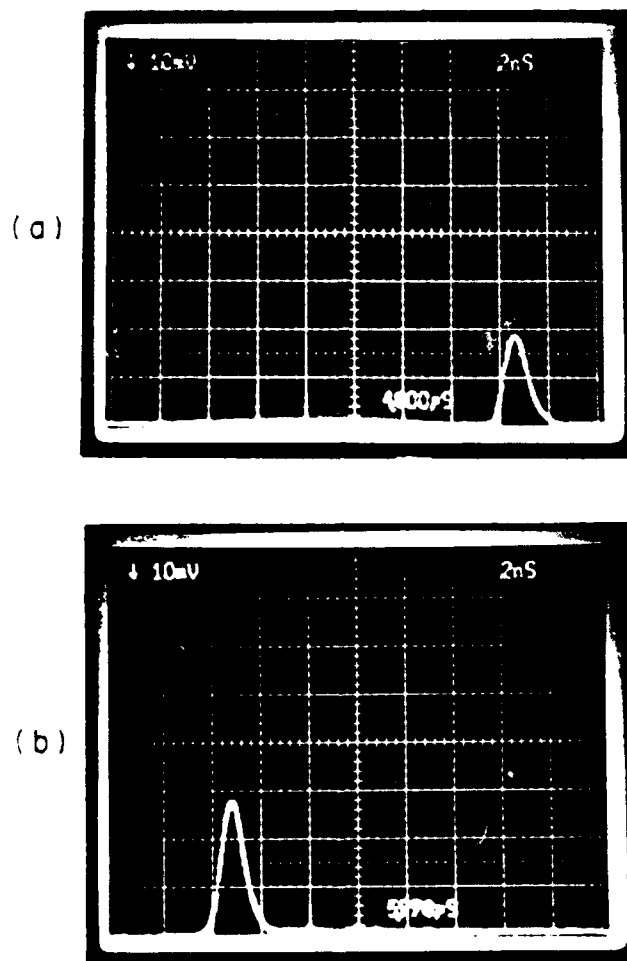
4.3 Measurements of Mode-Locked Pulse Duration

A) Using Photodetector

This set-up involved:

1. A fast magnetically biased HgCdTe detector (Boston Electronics Model P005-4) with a bandwidth of 500-800 MHz.
2. 60 cm length of SMA cable rated at 18 GHz.
3. Tektronix 7A29 pre-amplifier rated internally at 1000 MHz (0.35 nsec risetime) and yielding 750 MHz (0.47 nsec risetime) in the 7104 mainframe.
4. Polaroid photograph at sweep speed of 2 ns/div.

The anticipated risetime of this arrangement is approximately 0.5 nsec. In practice, pulses with a full width at half maximum (as photographed) of 0.95 nsec were the shortest observed, under optimum conditions of mode-locking (Figure 9). This allows us to place an upper bound on the system risetime of 0.475 nsec. Most of the frequency doubling measurements were made with a measured (FWHM) pulse width of 1.3 nsec, which is deconvoluted, using 0.475 nsec in quadrature, to 1.03 nsec. Because 1.3 nsec is not clearly larger than the system response time, there is quite a lot of uncertainty attached to this deconvolution. A second, more accurate,



P6478

Fig. 9 Oscilloscope traces of individual short pulses.

method of measurement involves autocorrelation using second harmonic generation, discussed in the following section.

b) Using Autocorrelation

In this technique the mode-locked CO₂ laser beam is split into two equal beamlets, one of which is delayed by varying amounts relative to the other before they are both superimposed within a nonlinear crystal. We chose a set-up in which both beams had the same polarization in order to utilize the 35 mm AgGaSe₂ crystal in the Type I phase matching configuration. This has the minor disadvantage that when one pulse is delayed by more than a whole pulse length from the other, there is still a background level of harmonic. Also, the two beams had to be tilted at a small angle to each other in order to avoid Michelson fringes which would otherwise give a fluctuating harmonic signal depending on the number of wavelengths of delay. We used an intersection angle of 0.005 rad, which yielded 3 fringes across the combined beam, in the horizontal direction, perpendicular to the polarization. The transverse distance between fringes was 2 mm, which exceeded the calculated "walk-off" distance (for SHG) of 0.35 mm, so that the whole length of the crystal was efficiency used. The total angle was less than half the available phase matching angle. Harmonic conversion efficiency was kept below 15% so as to be in the second power law regime. The expected autocorrelation waveform for Gaussian pulses is now derived.

Where Δ is the HWHM of the Gaussian pulses, the first and second pulses have the intensity waveforms:

$$I_1 = e^{-\frac{(\ell n 2)t^2}{\Delta^2}}$$

$$I_2 = e^{-\frac{(\ell n 2)(t - \tau)^2}{\Delta^2}}$$

where I_2 is delayed by time τ with respect to I_1 . The wave amplitudes are

$$E_1 = \sqrt{I_1} \text{ and } E_2 = \sqrt{I_2}$$

(in magnitude).

For beams superposed at a small angle the resultant amplitude is $(E_1 + E_2 \sin \phi)$ for $-\infty < t < \tau/2$ and $(E_2 + E_1 \sin \phi)$ for $\tau/2 < t < \infty$ where ϕ is a linear function of the transverse coordinate perpendicular to the lines of the fringes. It may be seen from Figure 10 (a) that there is time symmetry about $\tau/2$, so the total second harmonic energy is:

$$E_{SH} = \frac{1}{2\pi} \int_0^{2\pi} 2 \int_{-\infty}^{\tau/2} (E_1 + E_2 \sin \phi)^4 d\phi dt$$

where the average is taken over one whole fringe in the transverse direction. Expanding the bracket and integrating in ϕ gives:

$$E_{SH} = 2 \int_{-\infty}^{\tau/2} e^{\frac{-(2\ell n 2)t^2}{\Delta^2}} dt$$

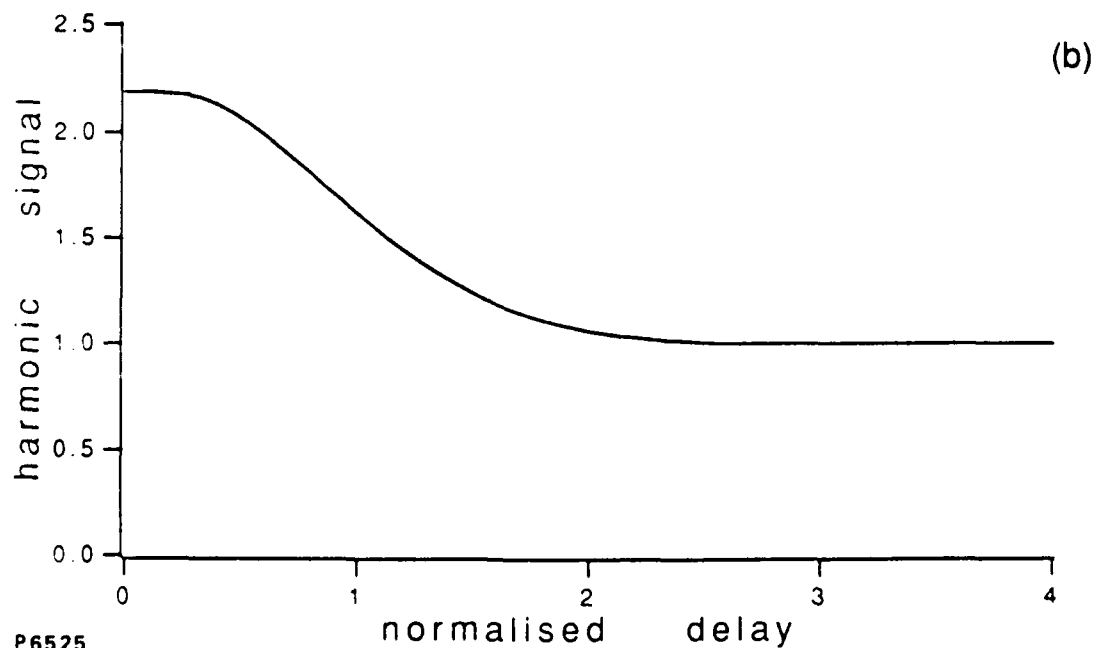
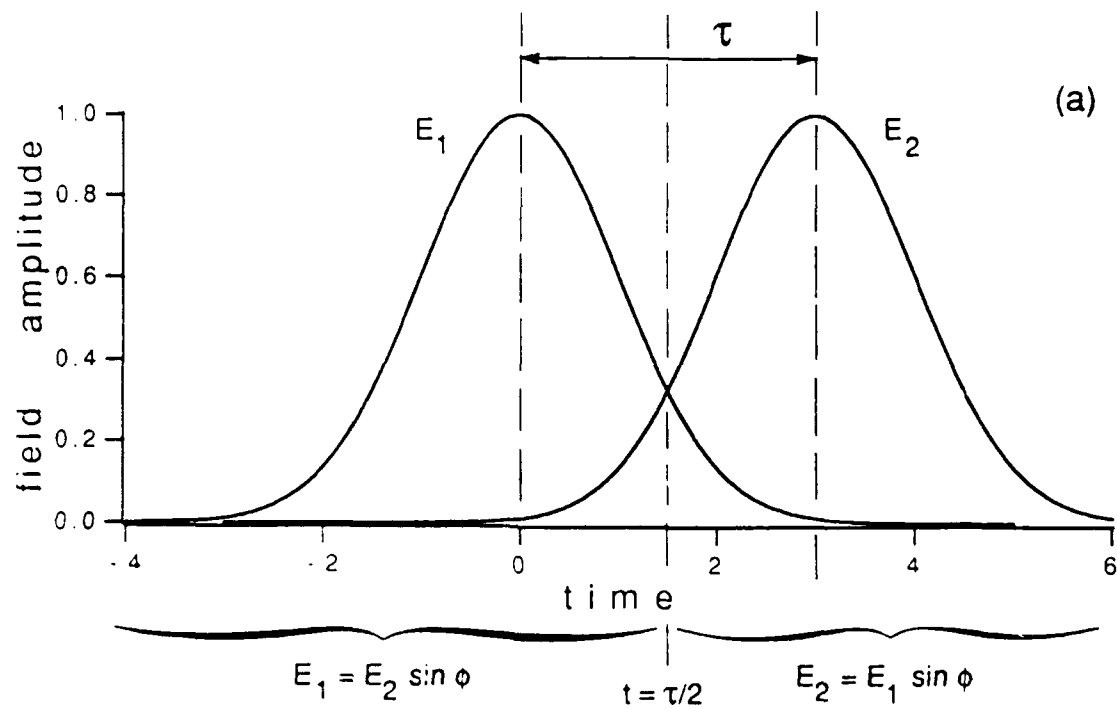
$$+ 6 \int_{-\infty}^{\tau/2} e^{\frac{-\ell n 2(t-\tau)^2}{\Delta^2}} dt$$

$$+ 0.75 \int_{-\infty}^{\tau/2} e^{\frac{-2\ell n 2(t-\tau)^2}{\Delta^2}} dt$$

This expression can be evaluated numerically as a function of τ/Δ (Figure 10 (b)) and compared with the measured autocorrelation profile to fit Δ (Figure 11). The limiting case of widely separated pulses ($\tau \gg \Delta$) gives

$$E_{SH} = \sqrt{\frac{2\pi}{\ell n 2}} \Delta,$$

which of course equals twice the second harmonic energy from an individual pulse $\left(2 \int_{-\infty}^{\tau/2} E_1^4 dt \right)$.



P6525

Fig. 10 (a) Derivation of autocorrelation integral using symmetry about time $\tau/2$. (b) Computed harmonic signal as a function of normalized delay τ/Δ where Δ is the HWHM of the Gaussian pulse.

For coincident pulses $E_{SH} = \frac{35}{16} \sqrt{\frac{2\pi}{\ln 2}} \Delta$, exceeding the background second harmonic by a factor of 2.1875.

This theory assumes that all of the emitted laser spectrum is mode-locked, so that there is temporal coherence throughout the laser pulse, for the leading and trailing parts of the pulse to interfere in a fringe pattern, regardless of the delay. The observed fringe pattern at most delays has a high contrast ratio (on heat sensitive paper, or liquid crystal polymer) so the condition appears to be satisfied. Additionally, the frequency spectrum of the mode-locked train is estimated to be a substantial fraction of the available gain bandwidth of the 1 atmosphere CO₂ laser medium, so that unlocked modes are not likely to be present.

The experimental autocorrelation profiles fit the theory reasonably well (Figure 11). Three determinations of the peak to background ratio gave an average of 2.2 ± 0.1 , in agreement with theory.

The measured pulse durations varied somewhat after different "tunings" of the laser, and averaged 0.90 ± 0.05 nsec, for the short pulse trains used in a detailed comparison of second harmonic with theory (Section 6.0).

4.4 Mode-Locking with Line Selection

Two methods were used to select the P-20 9.55 μm line chosen for this work, injection by CW laser and intracavity grating tuning. A description of each set-up is given in Section 3. In this section the suitability of each of these approaches for use with an intracavity modulator is discussed. The pulse durations measured by each approach were in fact indistinguishable, for comparable depth of modulation. The difference between them theoretically is that in the line injection case the initial intracavity flux has a much smaller bandwidth, expected to be of the order of 1 MHz, whereas in the grating case the initial (noise) bandwidth is on the order of 1 GHz. In each case the modulator is powered 200 μsec before the CO₂ gain medium is pulsed, so that in theory the intracavity line-injected radiation has some modulation prior to the appearance of gain. This effect is not very large, though, because the lifetime of cavity photons without gain is only a few round trips, compared to the eventual persistence of 50-100 round trips during the gain-switched buildup phase.

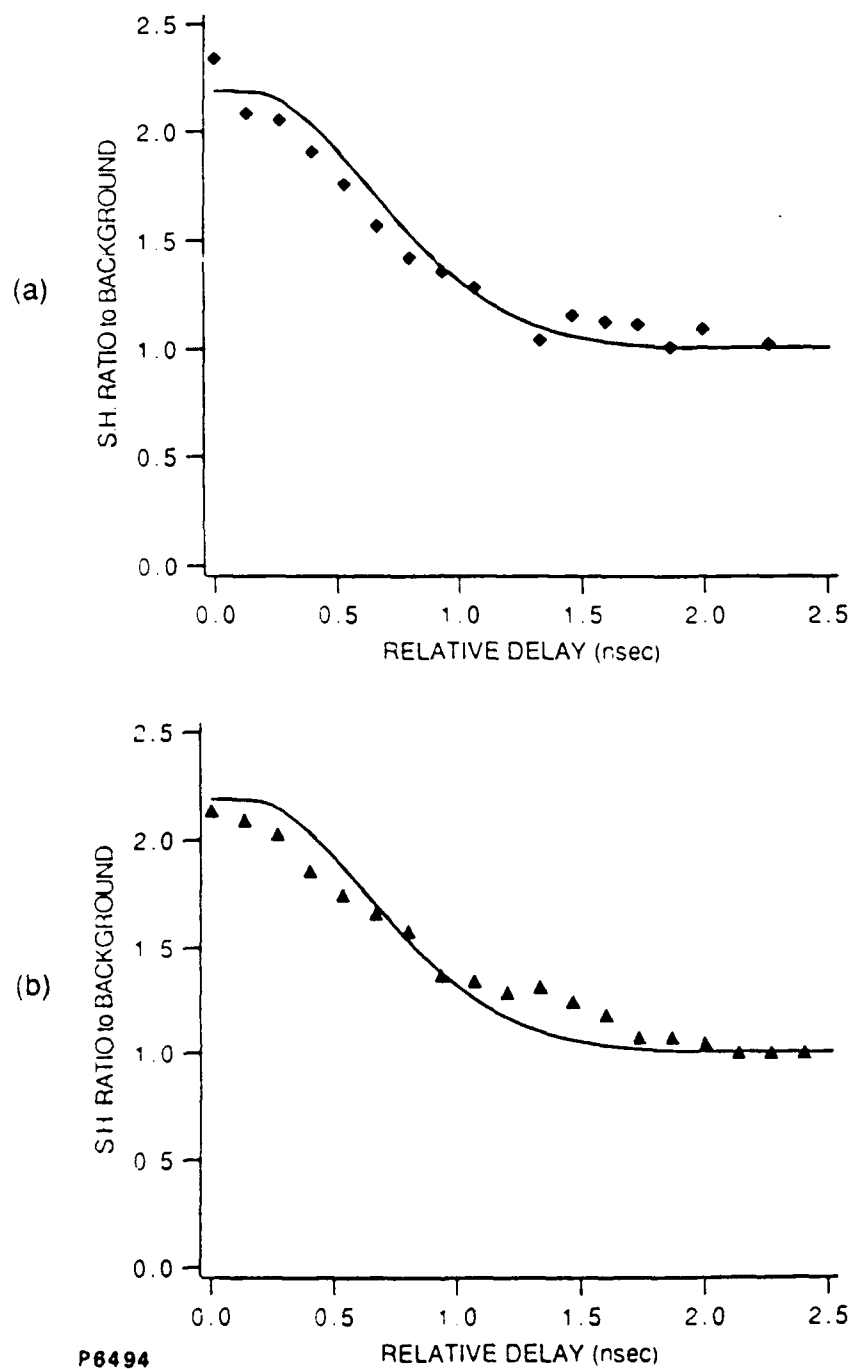


Fig. 11 (a) and (b) Two examples of the experimental autocorrelation data and superimposed theoretical curves of the type in Fig. 10 (b).

The 2 nsec structure present in an unmodulated grating-tuned laser (Figure 7) is the result of gain-narrowing during buildup. Most of this narrowing is due to the gain profile of the laser medium, but some of it is due to grating dispersion. Without this gain-narrowing the individual pulses would emerge from a modulated laser with a 1-2 nsec envelope (as in the line injection case) but there would be finer structure (0.1 nsec) within the envelope. For the CO₂ laser, the relatively narrow gain bandwidth ensures that with the present frequency and depth of modulation the resultant pulses are unstructured and of similar duration in both the line injection and grating tuned cases. This need not necessarily have been the case. For example, the line-injected and mode-locked Nd:YAG laser would not have structured pulses, but structure would usually be present in the grating-tuned version. In the transient mode-locking regime the duration of the pulse envelope would be much the same in each case.

One aspect relating to the use of a grating within a modulated cavity is that apparently the round trip time is different at different lateral positions on the grating (typically used at about 25° to normal). For a spot size of 0.6 cm, the difference in cavity round trip length is about 1 cm. First of all, the mode-locked pulse duration was experimentally insensitive to ± 0.5 cm variation in cavity length (out of a round trip length of 600 cm), but more importantly the modes of a cavity with a grating are more like "supermodes" in a distributed feedback resonator. The round trip length becomes "fuzzy" and the only effect to be considered is the small difference in cavity loss across the CO₂ laser line due to misalignment, because the grating only reflects "normally" at the central frequency.

4.5 Modulator Damage Threshold

The 1 cm thick Ge modulator crystals occasionally exhibited surface optical damage (probably to coatings) and at other times laser energy was down but could be restored by moving the modulator transversely to an unused position indicating possible volume damage, even although surface damage was not always visible.

Through trial and error it was found that hundreds to thousands of pulses could be obtained without apparent damage for intracavity fluences on the modulator of up to 0.45 J cm⁻². This result refers to mode-locked

pulse trains of 10-100 pulse duration, at peak intensities of 50-20 MW cm⁻², respectively.

The interpretation of these numbers is complicated by the fact that the modulator is very close to the grating at one end of the cavity and the 1 nsec pulses simultaneously pass through the modulator in both directions, each way having a fluence of 0.5 J cm⁻². The bench test of a modulator should be a single pass fluence of 1 J cm⁻². Further uncertainty comes from the likely existence of long duration standing waves in which the electric field maximum dwells locally in parts of the modulator.

Without anti-reflection coatings the Ge modulator would have (incoherent) surface losses of 36% per surface. Use of Brewster angle modulators is not practical because $\theta_B = 76^\circ$ and too large an optical footprint would result.

Damage to other elements in the optical cavity was only observed above the modulator threshold. The ZnSe Brewster angle windows of the oscillator withstood fluences of 1.5 J cm⁻² for hundreds to thousands of pulses. The grating showed what appeared to be a small amount of additional finely-distributed scattering in the area of irradiation at fluences above about 1 J cm⁻², but this did not appear to diminish its efficiency, and did not progress into more advanced damage.

5.0 ANGULAR AND TEMPERATURE DEPENDENCE OF PHASE-MATCHING

In a high average power application residual absorption can raise the temperature of the crystal, leading to refractive index changes which usually cause a loss of phase matching. There had been two reports^(20,15) of widely differing temperature dependence of the index difference in AgGaSe₂, so to resolve this conflict the low-intensity phase matching profile was established as a function of temperature for the doubling of mode-locked pulse trains at 9.55 μ m. This work was done with "hybrid" pulse trains consisting of a "spike" and "tail" of roughly equal energy, as illustrated in Figure 6. The harmonic conversion efficiency was about 5% for each of the experimental runs shown in Figure 12. The doubling was performed with a TEM₀₀ beam of 1/e² (intensity) radius = 0.50 cm, and almost plane wave front. The angular dependence of the doubling was due to the induced phase mismatch and not to angular components in the first harmonic beam.

In Figure 12 the continuous curves represent a least squares fit of the $(\sin \delta/\delta)^2$ function to the data points, with the appropriate scaling and offset parameters. Here

$$\delta = \frac{1}{2} \Delta k L$$

where L = crystal length and

$$\Delta k = k^{2w} - 2k^w = \frac{4\pi}{\lambda} (n_2^e - n_1^o)$$

where $\lambda = 9.55 \mu\text{m}$.

In four fitting procedures the mean value of

$$\frac{\partial}{\partial \theta} (n_2^e - n_1^o)_{\theta=\theta_m}$$

was established as -0.0325 ± 0.0025 per sterad, with the sign appropriate for θ increasing with increasing angle to the optic axis, θ being measured internal to the crystal.

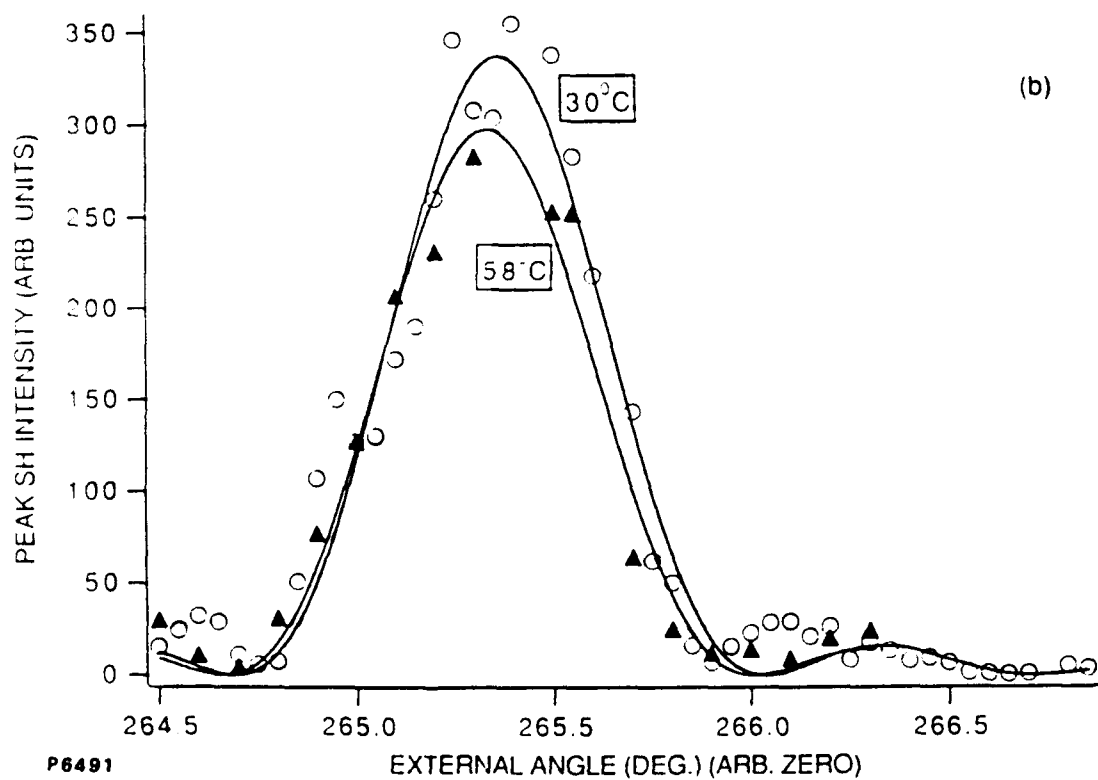
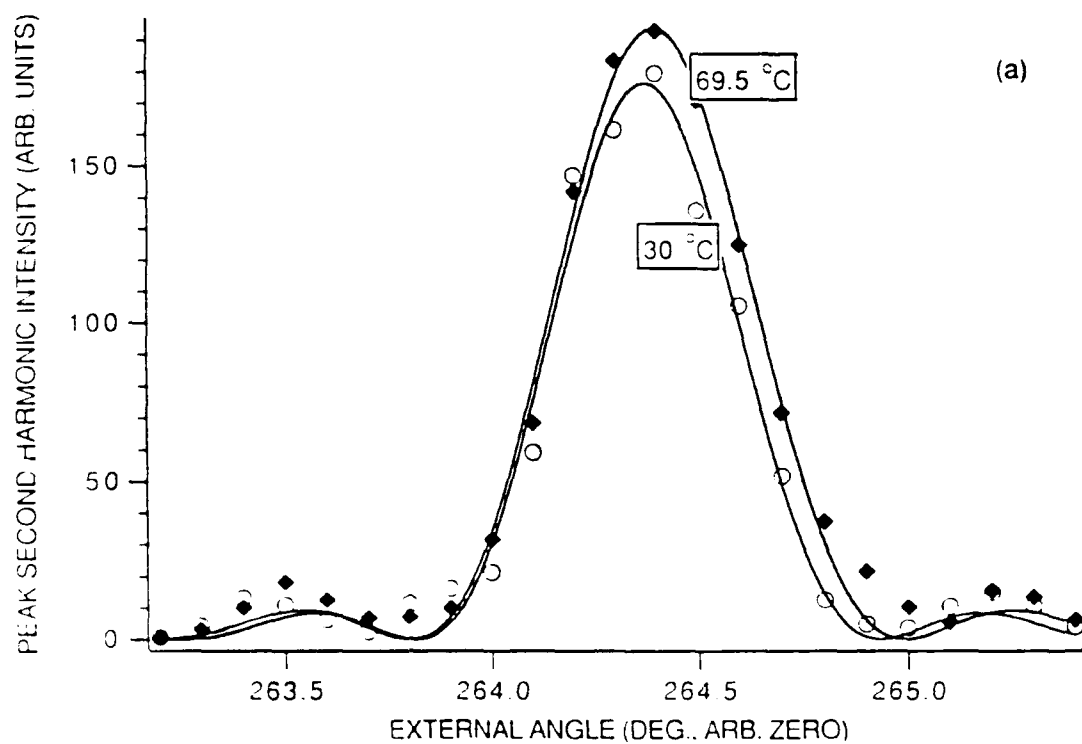


Fig. 12 (a) and (b) Temperature dependence of phase matching in two runs at low conversion.

The same quantity may be estimated theoretically, starting from the relation

$$\left(\frac{1}{n_2^e(\theta)}\right)^2 = \left(\frac{\cos\theta}{n_2^o}\right)^2 + \left(\frac{\sin\theta}{n_2^e}\right)^2$$

and differentiating with respect to θ

$$\frac{-2}{(n_2^e(\theta))^3} \frac{\partial n_2^e}{\partial \theta} = \frac{-2\cos\theta\sin\theta}{(n_2^o)^2} + \frac{2\sin\theta\cos\theta}{(n_2^e)^2}$$

Since $\frac{\partial n_1^o}{\partial \theta}$ is zero,

$$\frac{\partial}{\partial \theta} (n_2^e - n_1^o)_{\text{Theor}} = -0.0322$$

which is equal to the measured value above within the experimental error. For the record, the index for both "e" and "o" rays at the phase matching angle is 2.59693.

As may be seen in Figure 12, there is not any detectable change in the phase matching angle with temperature between 30°C and 70°C. In part (a) of that figure the matching is 0.025° (external) further from the C-axis at the higher temperature, with a fitting error of $\pm 0.02^\circ$. In part (b) the matching is $0.03^\circ \pm 0.02^\circ$ closer to the C-axis at the higher temperature. The average of these measurements is

$$\frac{\partial}{\partial T} (n_2^e - n_1^o)_{\theta=\theta_m} = 0 \pm 2 \times 10^{-7} \text{ K}^{-1}$$

The result is much lower than two previous determinations, which however relate to different wavelengths or temperature ranges. In reference (15), a value of $1.1 \times 10^{-6} \text{ K}^{-1}$ was determined for doubling of 10.6 μm between 100K and 298K, whereas in reference (20) a single wavelength of 3.39 μm was used, the temperature range was 100K to 300K and a value of $30 \times 10^{-6} \text{ K}^{-1}$ was obtained.

To conclude this section, the angular dependence of phase matching was exactly equal to that theoretically expected for a 3.5 cm crystal, indicating the absence of index flaws throughout its length. Furthermore, the temperature coefficient of the index difference was zero to within the experimental error, suggesting that we have accidentally hit upon a null at which the temperature coefficients of ordinary and extraordinary indices are exactly equal. Individually these coefficients are roughly in the range $40\text{-}70 \times 10^{-6} \text{ K}^{-1}$ at room temperature.⁽¹⁵⁾

5.1 Intensity Dependence of Phase-Matching

It is known that as the conversion efficiency into second harmonic is increased the process becomes more sensitive to small degrees of phase mismatch.^(21,12) This effect could readily be observed in the present experiments. Figure 13 contrasts the angular dependence of second harmonic efficiency at low conversion (about 5%) with that at high conversion (68% energy conversion at zero phase mismatch). The width of the central peak (at half height) has been reduced by a factor of 0.67 in this run, which refers to the longer pulse train shown in Figure 6, at an incident energy of 140 mJ. The secondary maxima are higher and closer to the central peak, in line with expectation. Another experimental run showing a width reduction by a factor of 0.57 is shown in Figure 14. This run had a smaller energy conversion efficiency at zero phase mismatch (56%) and employed the short pulse trains shown in Figure 6 at an incident energy of 70 mJ. The small differences between the two data sets could be due to deviations from Gaussian transverse profiles (Section 6.0) and possibly to the difference in the pulse train envelopes. Both sets are in qualitative agreement with theory ⁽²¹⁾ for pulses Gaussian in time and space. Although the theory was for a single pulse, the pulse train can be viewed as a sum of separate contributions which would closely approximate a single Gaussian if merged together. The angular range of incident light in these experiments was less than 0.1° (FWHM).

The narrowing of the phase-matching curve at high conversion is a factor to consider in the design of practical systems from two points of view. Firstly, the effects of a temperature rise following crystal absorption become

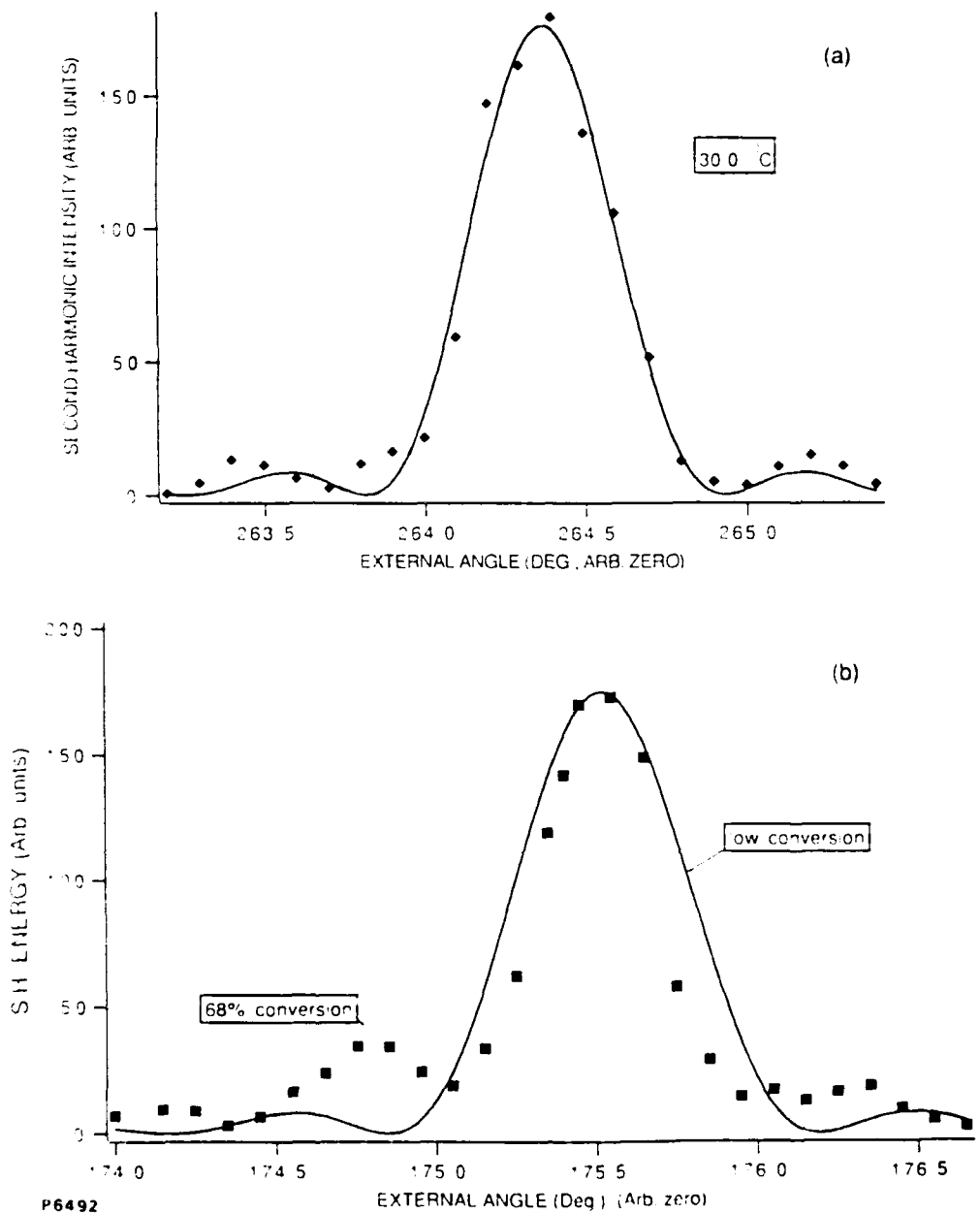


Fig. 13 (a) Low conversion phase matching curve. (b) 68% peak energy conversion narrowed phase matching curve, taken with 3 μ sec pulse trains.

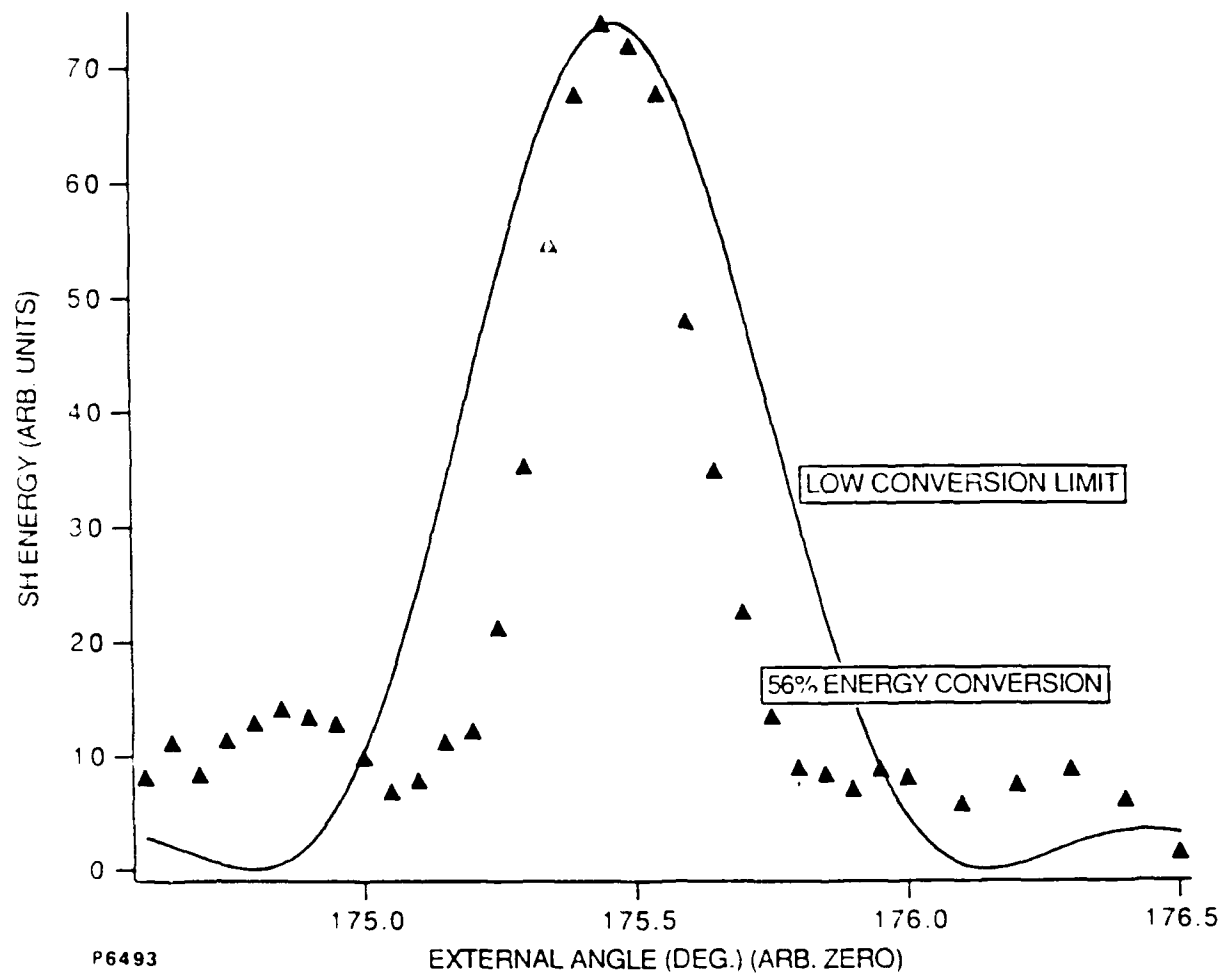


Fig. 14 56% peak energy conversion narrowed phase matching curve, contrasted with low conversion case. Taken with 0.3 μ sec pulse trains.

more critical and secondly, the angular acceptance for efficient doubling is restricted. In the present case, with a 3.5 cm crystal the achievement of > 50% conversion requires that external full angular width is less than about 0.13° . Crystal alignment also has to be more accurate.

6.0 HARMONIC GENERATION WITH SHORT PULSE TRAINS

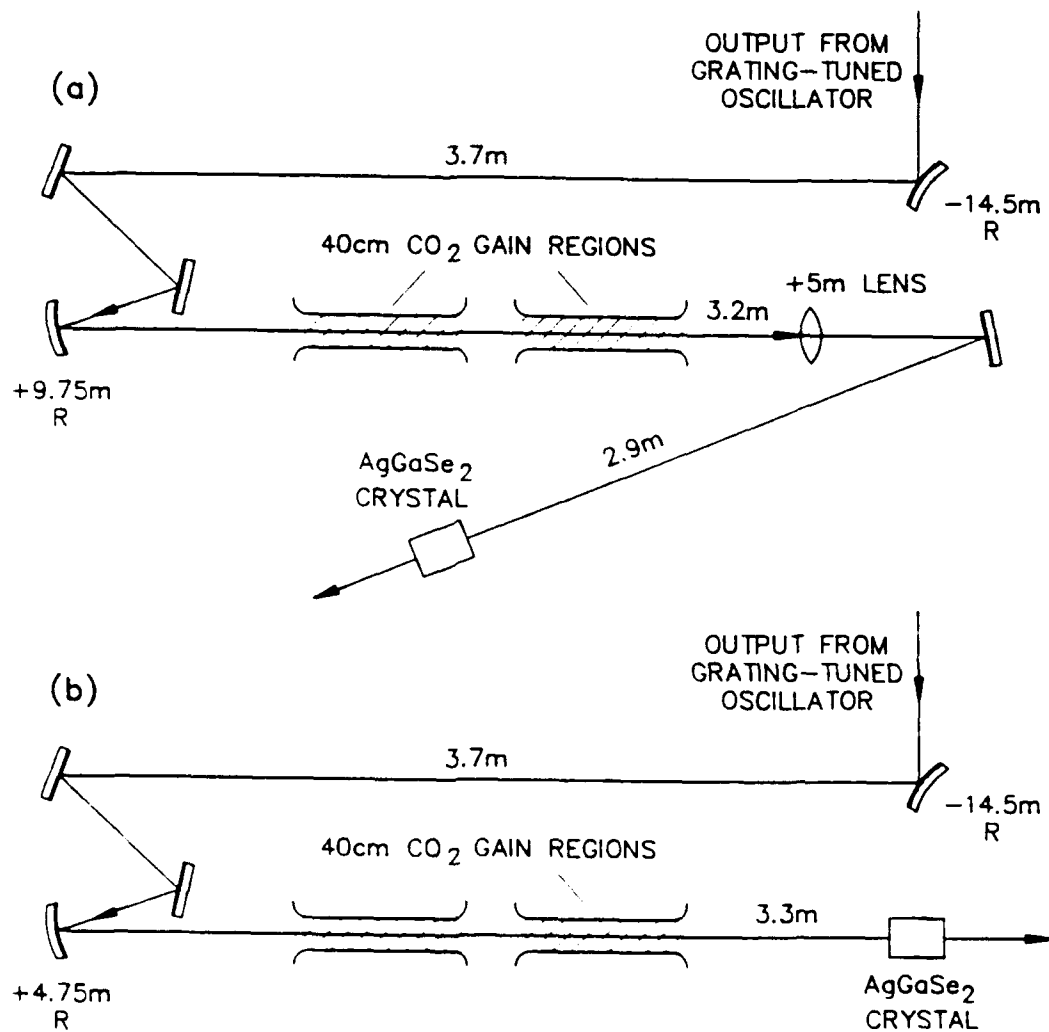
Short pulse trains obtained with the grating tuned oscillator (Section 3.2) were employed for a detailed comparison of second harmonic generation with theory. The duration of the short pulses was determined to be 0.90 ± 0.05 nsec by autocorrelation (Section 4.3 (b)). The pulse trains had a full width at half maximum of 0.30 μ sec and contained about 10 pulses spaced by 40 nsec. The maximum energy that could be obtained after amplifying one of these short pulse trains was 143 mJ.

Two configurations were employed, as shown in Figure 15. In each case the transverse profile of the pump beam was determined at the crystal location by measuring the fraction of the total energy transmitted through a range of different iris diameters. This data was least squares fitted to the transmission function anticipated for a Gaussian beam

$$T(a) = (1 - e^{\frac{-2a^2}{w^2}})$$

where a = radius of iris and $w = (1/e^2 \text{ intensity})$ radius of beam (Section 2.3). Figure 16 shows four measured profiles. Parts (a) and (b) of that Figure refer to the configurations in Figure 15 (a) and 15 (b) respectively, although the profile for Figure 16 (b) was taken with the amplifier turned off. The profiles are very close to Gaussian, with $1/e^2$ intensity spot parameters $w = 0.206$ cm and $w = 0.220$ cm in Figures 16 (a) and (b), respectively. When the amplifier is turned on, the near field profile (configuration of Figure 15 (b)) becomes distorted, as shown in Figure 16 (c) (solid circles). For comparison, Figure 16 (b) is shown again in part (c) (open circles). This distortion is due to the amplifier saturation being less for off-axis parts of the beam, leading to their relative increase. Although this configuration gave the highest fundamental energy (143 mJ) the presence of a relatively large low intensity "halo" gave lower harmonic generation efficiency than was obtained with the better profiles of the other configuration (Figure 15 (a)).

For the Figure 15 (a) configuration, examples of the fundamental and second harmonic pulse trains at 70% energy conversion are shown in



P2544

Fig. 15 (a) Focussed doubling configuration with 5 m lens; (b) Doubling configuration with direct convergence through amplifier.

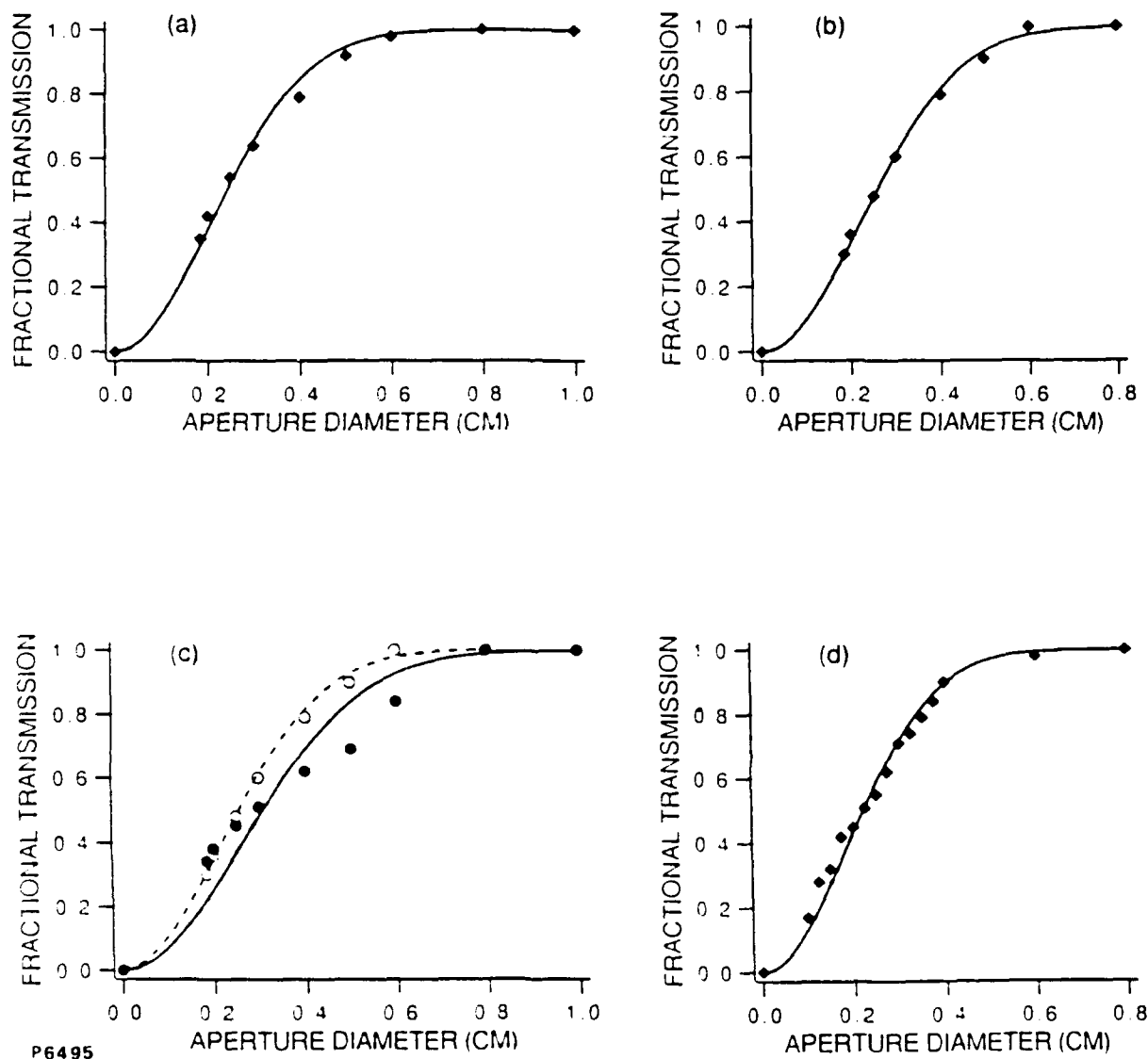


Fig. 16 9.55 μ m beam profiles determined at the crystal location by transmission through a variable aperture and fitted to Gaussian functions. (a) Configuration with 5m lens (Fig. 15 (a)); (b) configuration 15 (b) with turned off; (c) as in (b) (open circles) and with amplifier turned on (solid circles); (d) profile of long pulse trains generated in configuration 15 (b) with the amplifier on.

Figure 17. The depleted fundamental is also shown in Figure 17 (c), not exactly to scale because of a changed set-up.

In all cases the second harmonic was separated from the fundamental by passage at near-normal incidence through an uncoated 1 cm thickness of MgF_2 . It was verified using a spectrophotometer that this transmitted less than 0.5% at $9.55 \mu\text{m}$ and about 92% at $4.775 \mu\text{m}$. A MgF_2 correction factor of 1.08 was applied to all the second harmonic energies, which were measured on the same calorimeter as the fundamental energies. Energy data for the Figure 15 (a) configuration are shown in Figure 18.

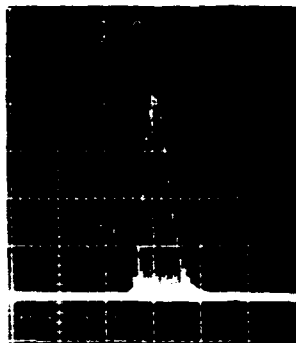
The second harmonic conversion formulae of Section 2.3 were applied to the present short pulse trains assuming that the pulse train itself had a Gaussian envelope in time. All the accurately known beam parameters were employed, surface entry and exit losses were accounted for, and the only variable was the nonlinear coefficient, d_{36} , of AgGaSe_2 . We show three values of d_{36} in Figure 18, to illustrate the probable range of values that fit the present data. The solid line and two dashed lines refer to $d_{36} = 31 \text{ pm V}^{-1}$ and $31 \pm 4 \text{ pm V}^{-1}$, respectively. Other literature values are listed in Section 2.4 and our present value agrees within errors with two out of four of them, tending to reinforce the lower literature values.

On the beam axis the peak intensity at the central point in a 140 mJ pulse train is 160 MW cm^{-2} . In the above configurations, the peak fluence is 2.0 J cm^{-2} . More detail is given on the surface optical damage threshold in Section 6.2. At the fluence of 2.0 J cm^{-2} , there was visible surface damage within three shots. However, at slightly lesser fluences hundreds of shots could be taken without damage.

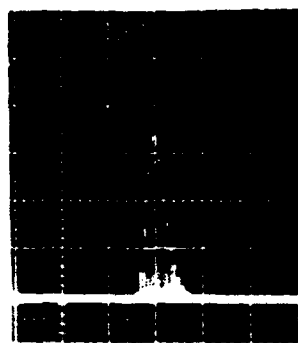
6.1 Harmonic Generation with Long Pulse Trains

In order to know whether the surface damage threshold is related more to intensity, or more to fluence, another doubling experiment was run with a much longer pulse train at lesser peak intensity. The $3 \mu\text{sec}$ pulse trains shown in Figure 6 were employed in the optical configuration of Figure 15 (b). The beam profile at the crystal is shown in Figure 16 (d). This profile is very close to Gaussian, showing a $1/e^2$ (intensity) radius $w = 0.188 \text{ cm}$. The difference from Figure 16 (c) is apparently due to the use of a larger mode-selection aperture for the generation of long pulse trains

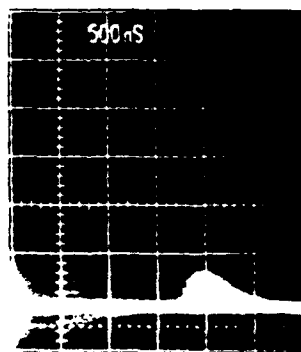
(a)



(b)



(c)



P6496

Fig. 17 Fundamental and harmonic pulse trains at 70% energy conversion. (a) $9.55\ \mu\text{m}$ intensity; (b) $4.775\ \mu\text{m}$ intensity; (c) depleted $9.55\ \mu\text{m}$ beam (not exactly to scale).

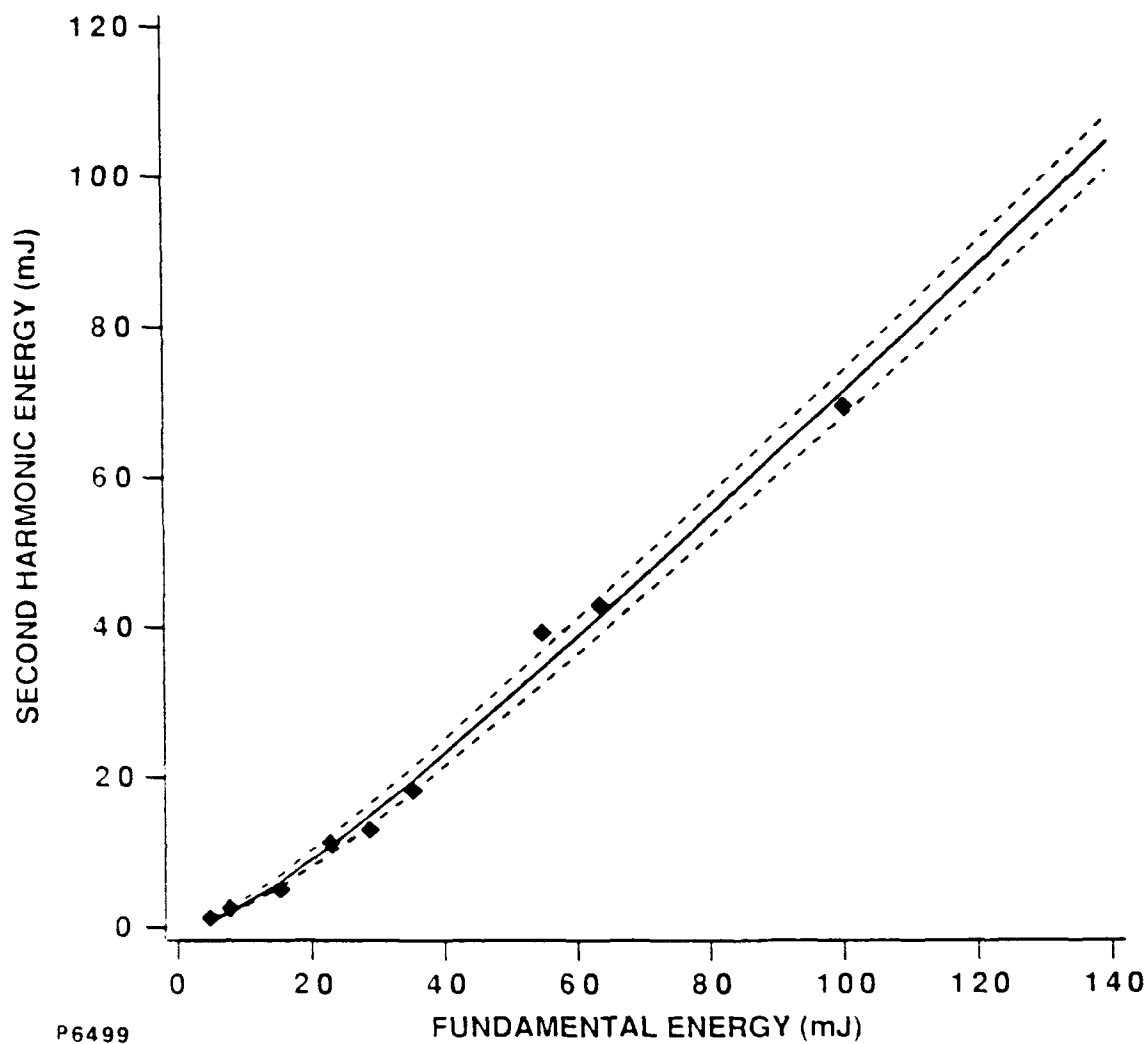


Fig. 18 Calculated and experimental second harmonic energy. Solid curve $d_{36} = 31 \text{ pm V}^{-1}$. Dashed curves $d_{36} = 31 \pm 4 \text{ pm V}^{-1}$.

in the oscillator (Section 3.2). The oscillator spot size is larger and hence the far-field spot is smaller.

The following table summarizes the harmonic conversion efficiency for long pulse trains at varying fluence.

Fundamental Energy (mJ)	Harmonic Energy (mJ)	Efficiency (%)	Fluence (number of pulses) J cm ⁻²
103.4 ± 2	50.2 ± 3	48.5 ± 4	1.86 (10)
156 ± 12	114.6 ± 5	73.5 ± 7	2.80 (6) occasional surface spark
200.7 ± 5	157	78	3.6 (1) 1 mm diameter of coating damaged
140	(generation of Phase matching curve at 62-68% conversion)		2.5 (80)

The highest harmonic conversion efficiency of 78% was observed on only one pulse because there was simultaneous surface damage at the entry face of the crystal. Conversion efficiency of 62-68% was obtained during a phase-matching measurement at a fluence of 2.5 J cm⁻² which the surface survived for at least 80 pulses. At the intermediate fluence of 2.8 J cm⁻² there were occasional small visible surface sparks on the crystal, which however did not lead to permanent damage because the same location was used for the (subsequent) phase matching measurement without further sparks.

The conversion efficiencies recorded in this long train experiment were just as high as those for the short train experiment, in spite of the use of much lower peak pulse intensities. One reason for this is that because of the profile of the pulse train a larger fraction of the pulses are of sufficiently high intensity to give efficient conversion. Using a result from Section 2.3 the peak Intensity I_0 in an individual pulse can be expressed in terms of the pulse energy E_p by

$$I_0 = \frac{2E_p}{\pi w^2 \Delta} \sqrt{\frac{\ln 2}{\pi}}$$

where Δ is the (HWHM) measure of pulse duration and w is the $1/e^2$ intensity radius of the beam. For the present 3 μ sec pulse train (75 pulses spaced by 40 nsec) the average peak intensity at 140 mJ total energy, assuming $\Delta = 0.45$ nsec as before and with $w = 0.188$ cm, is

$$I_0 = 33 \text{ MW cm}^{-2}$$

From Section 2.2 this corresponds to a peak drive parameter

$$\sqrt{\eta_0} = CL\sqrt{I_0} = 2.04 \text{ using } d_{36} = \text{pm V}^{-1}$$

and an average conversion efficiency (using Figure 1) of 58%. This is to be compared with an observed efficiency of 62-68% at the same fundamental energy. The apparent discrepancy could be due to a reduction in pulse duration through the pulse train because of continued modulation (discussed in Section 4.2). Although an autocorrelation experiment was not performed with the longer pulse trains, there is evidence from the direct detector/oscilloscope measurement that the pulse duration does decrease somewhat during the course of the pulse train. A reduction down to 0.7 nsec (FWHM) would have been sufficient to give the observed harmonic generation efficiency, but this lies below the detector/oscilloscope resolution.

6.2 Damage Threshold and Fluence Limitation

Although the damage threshold for AgGaSe₂ is often quoted as an intensity threshold (typically (22,14,23,15) in the range 10-30 MW cm⁻²) the present experiments with short pulse trains at up to 160 MW cm⁻² tend to indicate that fluence is more important than intensity for mode-locked pulse trains of less than 1 nsec pulse duration.

The harmonic generation experiments were performed at steadily increasing fluence until visible surface damage occurred. Both short (0.35 μ sec) and long (3 μ sec) pulse trains were used, in order to differentiate between the effects of intensity and fluence. Typical pulse train envelopes of

each type are illustrated in Section 3.2. In each experiment the transverse beam profile was characterized, as discussed above in Section 6.0, and the pulse duration was measured to be 1 ± 0.2 nsec in general, throughout the measurements. The damage observations are summarized in Table 2. For the short pulse trains the threshold for damage fluence lay between 1.45 J cm^{-2} and 1.58 J cm^{-2} whereas for the longer trains it lay between 2.5 J cm^{-2} and 2.8 J cm^{-2} . In view of the approximately 10 times greater peak intensity in the short pulse train, the relatively small reduction in damage fluence (0.6 times) indicates that fluence, rather than intensity, is the governing parameter in the surface damage of AgGaSe₂. This suggests that a critical surface temperature has to be reached for damage to occur, presumably the temperature at which sufficient conduction electrons are generated in the coating material to contribute a significant additional $9.55 \mu\text{m}$ absorption. Over the range of these measurements, the damage fluence can be empirically represented by

$$F_D = 2t^{0.25} \text{ Jcm}^{-2}$$

where t is the duration of the pulse train in μsec .

In other recent work⁽²⁴⁾ the damage threshold of coated and uncoated AgGaSe₂ was measured at $2.1 \mu\text{m}$ using 180 nsec laser pulses. An initial set of coated samples gave thresholds ranging from $1.4 - 2.5 \text{ J cm}^{-2}$. After re-polishing, the surfaces that had been re-coated (by a different vendor) gave thresholds ranging from $2.8 - 3.3 \text{ J cm}^{-2}$, whereas the uncoated surfaces ranged from $1.4 - 2.1 \text{ J cm}^{-2}$. The above data is not directly relevant to our own experiment in that the wavelength and pulse waveforms were very different. However, it illustrates that the precise details of surface preparation and coating can be important.

Table 2

Duration of Pulse Train (μsec)	Energy in Train (mJ)	$1/e^2$ Intensity Radius (cm)	Fluence (J cm^{-2})	Peak Intensity (MW cm^{-2})	Damage Y/N (no. of shots)
0.35	150	0.49	0.4	50	N(50)
0.35	180	0.40	0.7	110	N(10)
0.35	70	0.21	1.0	190	N(200)
0.35	100	0.21	1.45	270	N(25)
0.35	140	0.24	1.58	295	Y(1)
3	350	0.49	0.95	20	N(10)
3	140	0.19	2.5	30	N(80)
3	160	0.19	2.8	33	Y(3)
3	200	0.19	3.6	43	Y(1)

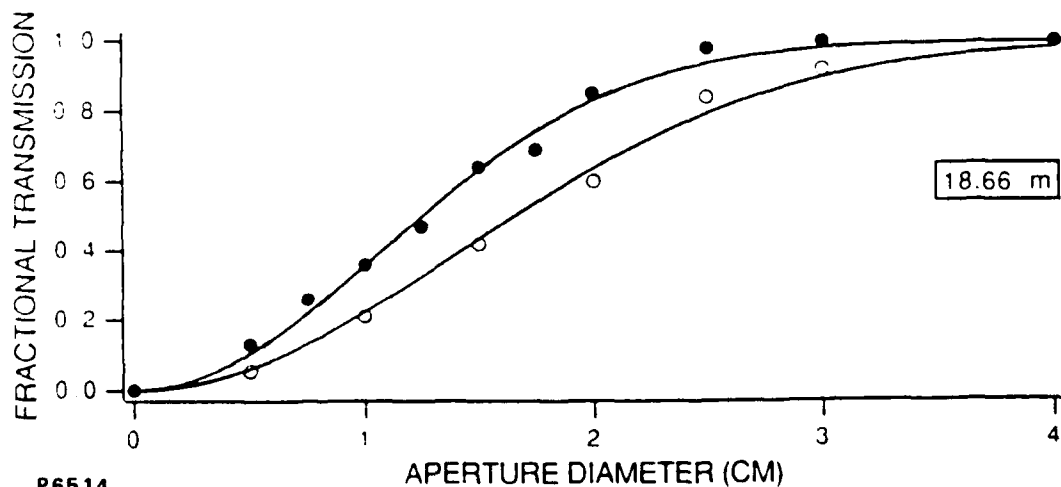
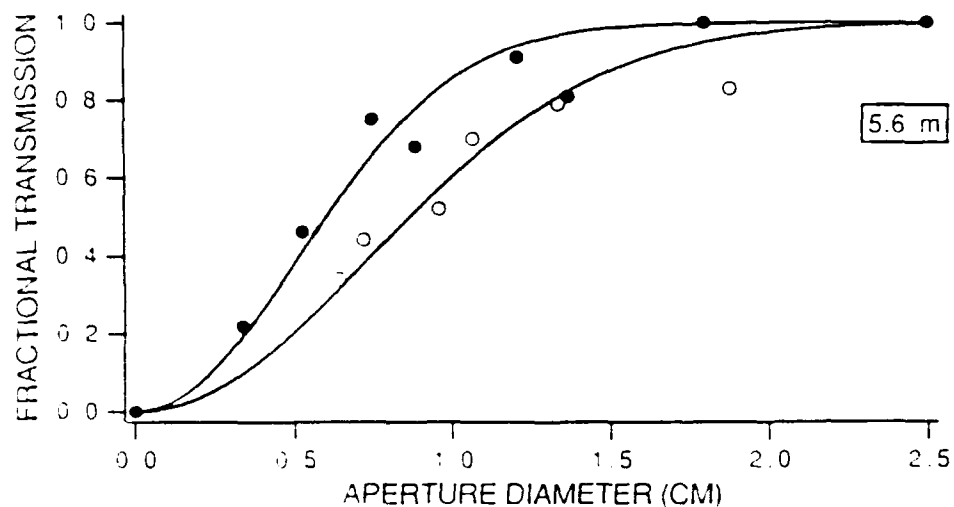
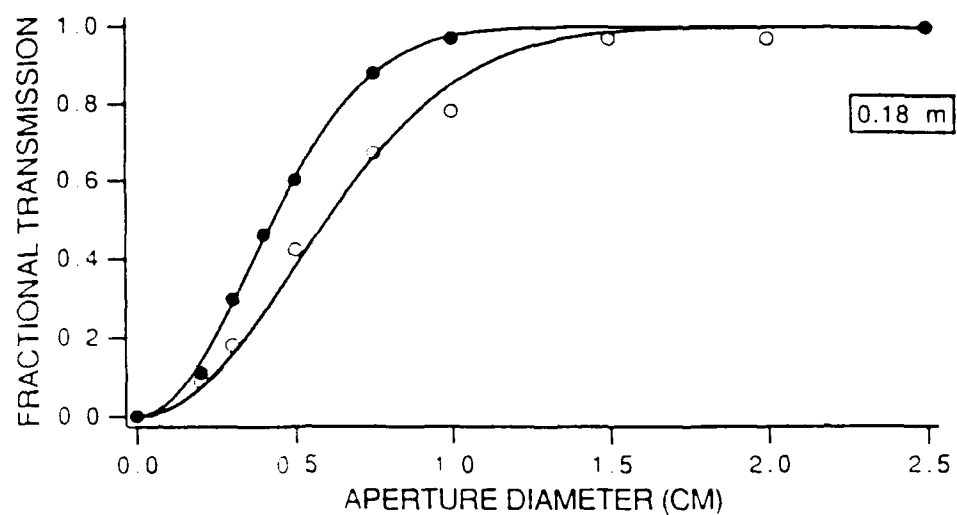
6.3 Optical Quality of Second Harmonic Beam

The use of a perfect single crystal of AgGaSe_2 (Section 5.0) and a diffraction limited TEM_{00} fundamental beam should have ensured a perfect second harmonic beam quality, and indeed this turned out to be the case.

Using a range of iris diameters, the fractional transmission of the fundamental and second harmonic beams was measured at three different distances beyond the crystal: 0.18 m, 5.6 m and 18.66 m. These corresponded to the near, intermediate and far fields for the $9.55 \mu\text{m}$ or $4.775 \mu\text{m}$ radiation. Typical data is shown in Figure 19. For these measurements the hybrid pulse train of Figure 6 (a) was employed, having 60% energy conversion efficiency in the leading spike, less than 10% conversion in the tail, and approximately 30% overall energy conversion.

The measured $1/e^2$ intensity spot parameters are summarized in Table (3).

The near field fundamental spot parameter was calculated from Gaussian beam resonator and propagation theory.⁽²⁵⁾ The near field second harmonic spot was calculated in the approximation that walk-off distances were small compared to the fundamental beam diameter, that is, by considering the conversion of a series of pulses Gaussian in time but like



P6514

Fig. 19 Beam profiles determined at various distances beyond the crystal by transmission through a variable aperture. Solid circles 4.775 μm beam, open circles 9.55 μm beam, Gaussian curve fit.

a plane wave in space, with amplitude appropriate to the radial location. The necessary formalism is discussed in Section 2.3.

The intermediate and far field fundamental spot parameters were calculated from resonator theory, plus propagation. In the far field the measured spot parameter agreed with theory to within 4%. For the second harmonic, the intermediate and far field spot parameters were calculated from the measured near field spot parameter, together with the assumption that the phase front of the second harmonic had the same (very slight) curvature as the fundamental. Again, the agreement was very good, although in the far field the measured spot was 11% larger than expected on the basis of Gaussian propagation theory, possibly due to the small fraction of the harmonic (less than 16%) that originated from the tail portion of the hybrid pulse, and would have been generated with a slightly smaller spot size. The far field spot contained $90\% \pm 10\%$ of the near field energy.

Table 3 Summary of Beam Quality Data

Distance From Crystal (m) (Frequency)	Measured Spot Parameter (cm)	Calculated Spot Parameter
0.18 (v)	0.49	0.50 From Resonator Theory
0.18 (2v)	0.37	~ 0.37 From SHG Theory
5.6 (v)	0.72	0.65 Propagation Theory
5.6 (2v)	0.51	0.48 Propagation Theory*
18.66 (v)	1.45	1.39 Propagation Theory
18.66 (2v)	1.08	0.95 Propagation Theory*

*From measured 0.18 m 2v spot size.

7.0 THERMAL CONDUCTIVITY OF AgGaSe₂

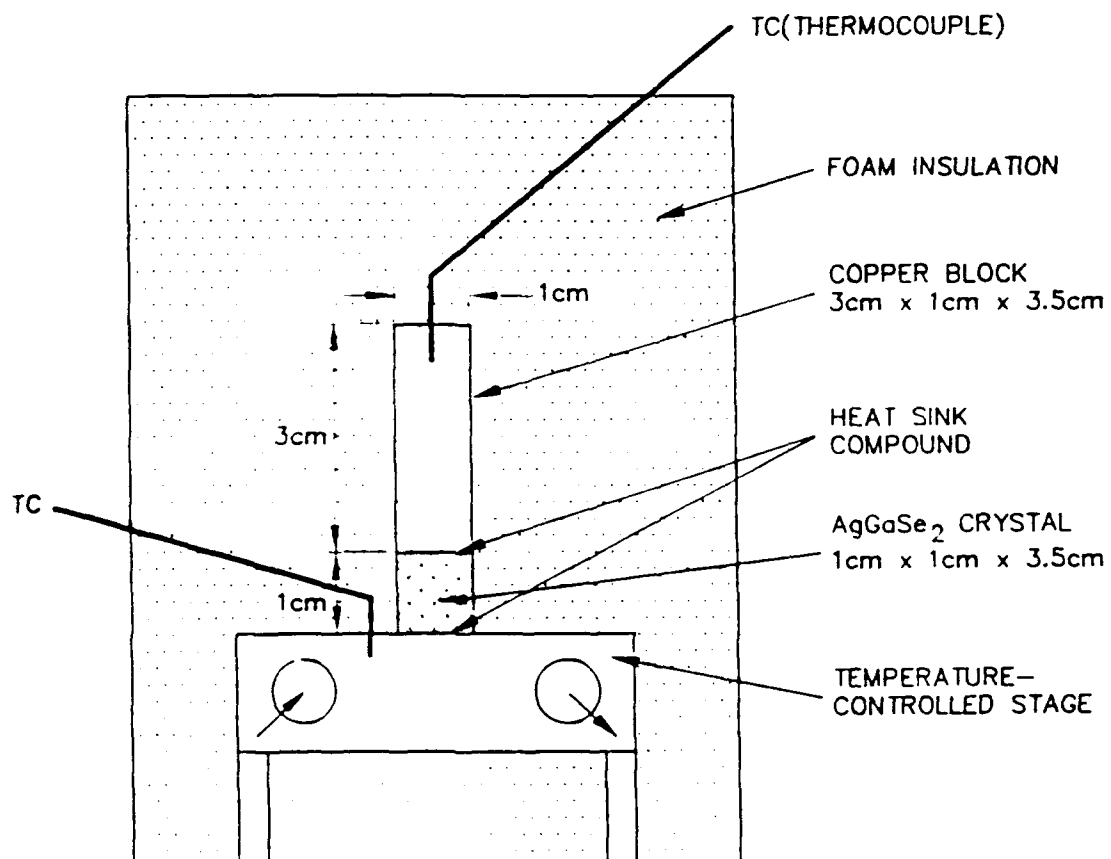
There are residual absorptions in AgGaSe₂ associated with either small inclusions, infrared overtones, or band edge sites, which cause crystal heating under high average optical power conditions. The crystal thermal conductivity, which determines the transverse (or longitudinal) crystal scale size that can be used, had not apparently been measured prior to the present work.

A simple experiment was devised to measure the (relatively low) thermal conductivity. A mass of copper (99.8 g) was contacted via the AgGaSe₂ crystal (10 mm x 10 mm x 35 mm) to a temperature-controlled stage as shown in Figure 20. Thermal contact was assured by using thin films of heat sink compound between the aluminum stage, the crystal and the copper. Light foamed plastic was used all around for thermal insulation and the temperatures of the stage and the copper block were monitored by digital thermocouples.

The measurement method involved a period of stabilization followed by a change of the stage temperature to a new value, either above or below the original value by 10 to 15°C. The temperature of the copper block was then followed to its new equilibrium, achieved, in the case of perfect insulation, only due to heat flow through the crystal. The temperature difference between the copper block and the stage decays according to

$$\Delta T = \Delta T_0 e^{-\left(\frac{\text{area} \times \text{thermal conductivity}}{\text{heat capacity} \times \text{crystal width}} \right) t}$$

where ΔT_0 is the initial temperature difference. Here, the area of the crystal is 3.5 cm² and the heat capacity is that of the copper (38.44 J/°C) plus a contribution from the crystal itself. The heat capacity of AgGaSe₂ is⁽²⁶⁾ 1.8 J cm⁻³/°C, i.e., 6.3 J/°C for the entire crystal. Initially there is an approximately linear temperature gradient between the stage and the copper block so that 3.15 J/°C is the effective heat capacity of the crystal, where temperature change on the block side of the crystal is concerned. The heat in the crystal has an average of only 2/3 of the crystal to traverse, so its effect is equivalent to only $2 \times 3.15/3 = 2.1$ J/°C if lumped with the heat



P2538

Fig. 20 Arrangement for the measurement of thermal conductivity.

capacity of the copper. The combined effective heat capacity of the crystal and the copper is therefore $38.44 + 2.1 = 40.54 \text{ J/}^\circ\text{C}$.

Typical temperature decays for each crystal orientation are shown in Figure 21. In one case the conductivity is perpendicular to the C-axis, and in the other it is at $(90-50.11) = 39.89^\circ\text{C}$ to the C-axis, i.e., mostly parallel to it. There is no significant difference between the temperature decay times for either of these orientations. The data from 6 runs are therefore lumped together to yield an average experimental decay time of $934.3 \pm 26.4 \text{ sec}$. From this, the conductivity at 25°C is

$$K = \frac{40.54}{3.5 \times 934.3} = 0.0124 \pm 0.0004 \text{ W cm}^{-1} \text{ } ^\circ\text{C}^{-1}$$

This is a relatively low conductivity, comparable to that for pyrex or fused silica. Fortunately, the temperature dependence of the phase mismatch for doubling to $4.775 \mu\text{m}$ is almost zero (Section 5.0), so that temperature excursions of more than 100°C can readily be tolerated. Further discussion of the use of AgGaSe_2 for high average power frequency multiplication is given in the following section.

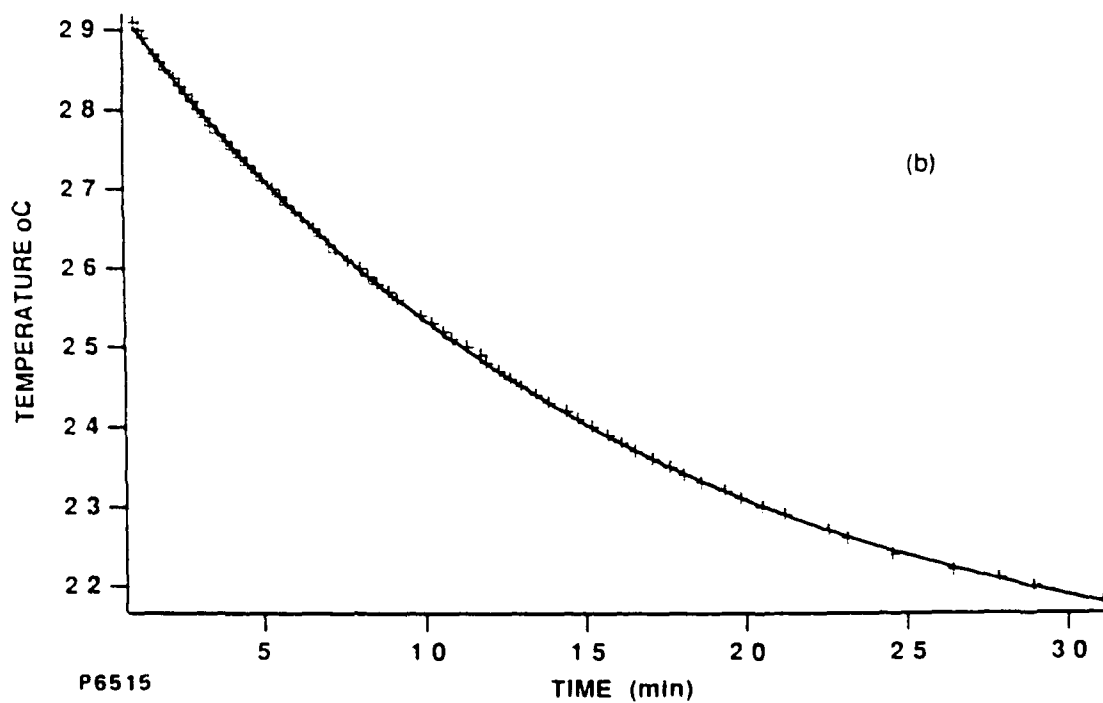
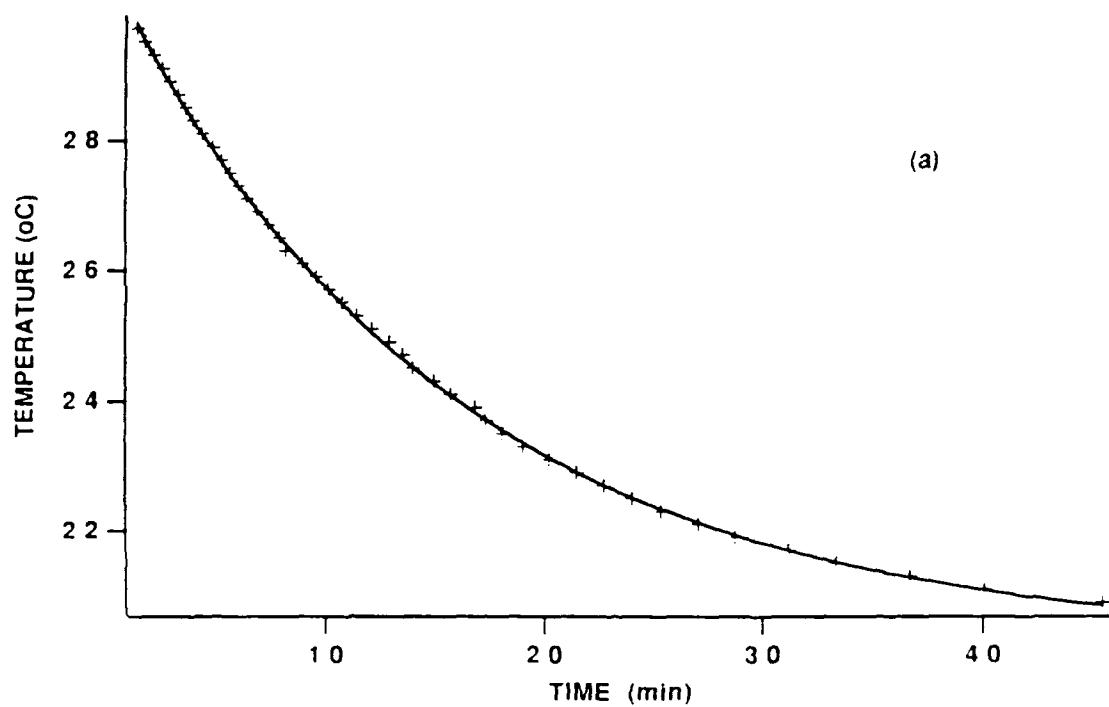


Fig. 21 Two examples of measured copper block temperature decays and their fitting to an exponential function.

8.0 HIGH AVERAGE POWER DOUBLING

In this section, we will briefly address some of the issues relating to high average power doubling in AgGaSe₂. The only limitation is crystal heating due to absorption at either 9.55 μm or 4.775 μm . For the typical case in which the length of the crystal greatly exceeds its transverse dimension a radial temperature profile is set up between the axis of propagation and the outside surface of the crystal. The refractive index increases with temperature ^(15,20) so a positive lens is formed. At sufficiently high internal temperature, differential thermal expansion causes stresses which will ultimately crack the crystal. An estimate of the maximum temperature differential for AgGaSe₂ is 100-200°C, derived by Eimerl et al.⁽²⁷⁾

In order to estimate the temperature rise, consider a cylindrical crystal of radius a and thermal conductivity K subject to a uniform volume heating rate A_0 (W cm^{-3}). If the length of the cylinder is much greater than its diameter and the outer cylindrical wall is kept at temperature T_0 then the steady state temperature profile as a function of radius is⁽²⁸⁾

$$T(r) = T_0 + \frac{A_0(a^2 - r^2)}{4K}$$

In reality the heating rate will not be uniform throughout the crystal because the beam intensity varies radially and the fundamental and second harmonic absorption coefficients will be different, leading to a variation with length. Although the present experiments used a Gaussian radial intensity profile, it would be better from the standpoint of efficient utilization of crystal material to use a "super-Gaussian" profile, which begins to approximate a constant volume heating rate. As it happens, the 9.55 μm and 4.775 μm absorptions in the present AgGaSe₂ sample are both about 1.5% per cm, so that a rough approximation to the crystal temperature rise can be obtained by assuming that the heat input is also constant along the crystal length.

For the above temperature profile there is a refractive index profile

$$n(r) = n_0 + \alpha(T(r) - T_0)$$

where $n(r)$ is the index at radius r , n_0 is the index at radius a and temperature T_0 , and α is the coefficient of refractive index with temperature. This is only an approximate estimate because in a cylindrical geometry there are stresses leading to compression of the central material and rarefaction of the outer shell, resulting in a modified index profile. The expansion of AgGaSe₂ is anisotropic⁽²⁹⁾ having in fact a negative coefficient parallel to the c -axis and a positive coefficient perpendicular to the c -axis.

Considering only the thermal dependence of the index the focal length of the equivalent lens can be calculated. For a thin lens of radius a with one surface plane and the other of radius R the thickness is closely approximated by

$$t(r) = \frac{1}{2R}(a^2 - r^2)$$

If it is made of a material of refractive index μ , the optical thickness at radius r is $t(r)(\mu-1)$, which is to be equated to $L_c [n(r)-n_0]$ from the thermal lens in a crystal of length L_c . Using the above expressions and the relationship $f = R/(\mu-1)$ for the focal length f of the thin lens, we obtain

$$f_c = \frac{2K}{L_c \alpha A_0}$$

for the focal length of the thermally induced lens in the crystal. In terms of the absorption coefficient of the crystal, α_0 , the heat input is $A_0 = I_0 \alpha_0$ where I_0 is the (assumed uniform) incoming laser intensity. Then

$$f_c = \frac{2K}{L_c \alpha I_0 \alpha_0}$$

For example, with

$$K = 0.0124 \text{ W cm}^{-1} \text{ K}^{-1}$$

$$L_c = 3.5 \text{ cm}$$

$$\alpha = 30 \times 10^{-6} \text{ K}^{-1}$$

$$I_0 = 200 \text{ W cm}^{-2}$$

$$\alpha_0 = 0.015 \text{ cm}^{-1}$$

we have $f_c = 79 \text{ cm}$.

The temperature rise at the center of the crystal relative to the (cylindrical) edge is

$$T(0) - T_0 = \frac{A_0 a^2}{4K} = \frac{I_0 \alpha_0 a^2}{4K}$$

This now depends on the crystal radius a . For the above example, with $a = 0.5$ cm, the central temperature rise is 15°C .

The effect of temperature upon phase-matching is discussed in Section 5.0 above. As shown there, the doubling process is completely insensitive to temperature, at least over the first 50°C above room temperature. It appears that the most significant phenomenon at high average power will be the formation of a positive lens in the crystal. To the extent that this lensing action begins to induce angular deviations in the beam, the phase matching will be affected, particularly at high conversion efficiencies (Section 5.1). For phase matching to be preserved, the angle a/f_c should remain less than about 0.2 degrees (3.5×10^{-3} radius).

9.0 REFERENCES

1. C. B. Moore, R. E. Wood, B-L Hu, and J. T. Yardley, J. Chem. Phys. 46, 4222 (1967).
2. G. D. Boyd, H. M. Kasper, J. H. McFee and F. G. Storz, IEEE J. Quantum Electr. QE-8, 900 (1972).
3. D. S. Chemla, P. J. Kupecek, D. S. Robertson and R. C. Smith, Opt. Comm. 3, 29 (1971).
4. R.C.Y. Auyeung, D. M. Zielke and B. J. Feldman, Appl. Phys. B48, 293 (1989).
5. D. R. Suhre, Appl. Phys. B52, 367 (1991).
6. G. D. Boyd, E. Buehler and F. B. Storz, Appl. Phys. Lett. 18, 301 (1971).
7. Yu. M. Andreev, V. Yu Baranov, V. G. Voevodin, P. P. Geiko, A. I. Gribenyukov, S. V. Izyumov, S. M. Kozochkin, V. D. Pis'menniy, Yu., A. Satov and A. P. Strel'tsov, Sov. J. Quant. Electron. 17 (11), 1435 (1987).
8. J. E. Midwinter and J. Warner, Brit. J. Appl. Phys. 16, 1135 (1965).
9. G. C. Bhar, Applied Optics 15, 305 (1976).
10. H. Kildal and J. C. Mikkelsen, Optics, Comm. 9, 315 (1973).
11. D. Roberts, private communication.
12. D. Eimerl, IEEE J. Quant. Electron., QE-23, 575 (1987).
13. J. A. Armstrong, N. Bloembergen, N. Ducuing and P. S. Pershan, Phys. Rev. 127, 1918 (1962).

REFERENCES (Cont'd.)

14. R. C. Eckhardt, Y. S. Fan, R. L. Byer, R. K. Route, R. S. Feigelson and J. van der Laan, Appl. Phys. Lett. 47, 786 (1985).
15. N. P. Barnes, D. J. Gettemy, J. R. Hietanen and R. A. Iannini, Applied Optics 28, 5162 (1989).
16. R. K. Route, R. S. Feigelson, R. J. Raymakers and M. M. Choy, J. Cryst. Growth 33, 239 (1976).
17. See for example, A. J. Alcock and P. B. Corkum, Phil. Trans. R. Soc. Lond. A298, 365 (1980).
18. R. L. Abrams and D. A. Pinnow, J. Appl. Phys. 41, 2765 (1970).
19. D. J. Kuizenga, D. W. Phillion, T. Lund and A. E. Siegman, Optics Comm. 9, 221 (1973).
20. N. P. Barnes, R. C. Eckhardt, D. J. Gettemy and L. B. Edgett, IEEE J. Quantum Electron. QE-15, 1074 (1979).
21. R. C. Eckhardt and J. Reintjes, IEEE J. Quant. Electron. QE-20, 1178 (1984).
22. H. Kildal and G. W. Iseler, Applied Optics 15, 3062 (1976).
23. R. C. Eckhardt, Y. X. Fan, R. L. Byer, C. L. Marquardt, M. E. Storm and L. Esterowitz, Appl. Phys. Lett. 49, 608 (1986).
24. B. C. Ziegler and K. L. Schepler, Applied Optics 34, 5077 (1991).
25. H. Kogelnik and T. Li, Applied Optics 5, 1550 (1966).

REFERENCES (Cont'd.)

26. H. Neumann, G. Kuhn and W. Moller, Crystal Res. and Tech. 20, 1225 (1985).
27. D. Eimerl, J. Marion, E. K. Graham, H. A. McKinstry and S. Haussuhl, IEEE J. Quant. Electron 27, 142 (1991).
28. "Conduction of Heat in Solids", Second Ed., H. S. Carslaw and J. C. Jaeger, Oxford Clarendon Press (1959).
29. I. V. Bodner and N. S. Orlova, Inorganic Matl. 25, 330 (1989).